



HAL
open science

Melt/rock ratios and melt fluxes during reactive percolation: from matrix- to melt-controlled dynamics

Valentin Basch, Marguerite Godard, Andrea Tommasi, Elisabetta Rampone

► To cite this version:

Valentin Basch, Marguerite Godard, Andrea Tommasi, Elisabetta Rampone. Melt/rock ratios and melt fluxes during reactive percolation: from matrix- to melt-controlled dynamics. Contributions to Mineralogy and Petrology, 2024, 180 (1), pp.6. 10.1007/s00410-024-02194-1 . hal-04845006

HAL Id: hal-04845006

<https://hal.science/hal-04845006v1>

Submitted on 18 Dec 2024

HAL is a multi-disciplinary open access archive for the deposit and dissemination of scientific research documents, whether they are published or not. The documents may come from teaching and research institutions in France or abroad, or from public or private research centers.

L'archive ouverte pluridisciplinaire **HAL**, est destinée au dépôt et à la diffusion de documents scientifiques de niveau recherche, publiés ou non, émanant des établissements d'enseignement et de recherche français ou étrangers, des laboratoires publics ou privés.



Distributed under a Creative Commons Attribution - NonCommercial - NoDerivatives 4.0 International License

Melt/rock ratios and melt fluxes during reactive percolation: from matrix- to melt-controlled dynamics

Valentin Basch^{1,2}  · Marguerite Godard³ · Andrea Tommasi³ · Elisabetta Rampone⁴

Abstract

Deep melt migration processes occurring beneath spreading ridges largely occur by porous flow and involve reaction with the pre-existing crystal matrix. The control of the melt/rock ratios and melt fluxes involved in these reactive percolation processes on the structural and chemical evolution of oceanic magmatic systems is yet to be fully constrained. We here report a combined petro-geochemical study of variably evolved gabbroic layers in the Oman Moho Transition Zone, atop the Maqсад mantle diapir, ranging from dunites, troctolites and wehrlites to olivine gabbros. The layering characterizing the base of the crustal section formed during a process of reactive porous flow and hybridization of a dunitic precursor. Positive feedback between melt distribution and deformation focusing allowed for the development of two distinct percolation behaviours, between focused melt percolation and diffuse melt impregnation. This geological setting provides an ideal case study to assess the impact of the melt/rock ratios and percolation dynamics on the evolution of textures and chemical compositions during focused and diffuse percolation. Namely, the former leads to a modification of the crystallographic preferred orientation and complete chemical reequilibration of the matrix, while the latter allowed for preservation of the pre-existing structure and buffer of the melt composition by the matrix and reactive processes. We quantify the melt/rock ratios associated with the two magmatic systems using *Plate Models* to demonstrate that focused percolation easily resets the matrix composition from melt/rock ratios integrated over time $\sim 2-3$, whereas diffuse, low-flux melt impregnation would require elevated melt/rock ratios (> 20) to allow for chemical reequilibration. Furthermore, we provide a global overview of the evolution of mineral compositions and textures of a percolated olivine-rich protolith as a function of the melt migration style and the involved melt/rock ratios, both instantaneous and integrated over time.

Keywords Reactive porous flow · Melt/rock ratio · Focused reactive percolation · Diffuse melt impregnation · Chemical reequilibration

Introduction

Oceanic lithosphere is continuously accreted along mid-ocean ridges, either by magmatic addition or by tectonic extension and exhumation as commonly observed at slow-spreading ridges (e.g., Dick et al. 2006). The extensive magma supply characterizing fast-spreading ridge environments leads to the formation of a Penrose-type stratified oceanic crust, up to 6 km in thickness (e.g., Boudier and Nicolas 1985; Niu 2021). The upper third of this crust is composed of pillow basalts and sheeted dikes (Teagle et al. 2006) that are fed by a relatively stable axial melt lens at their base (e.g., France et al. 2021 and references therein). On the other hand, the lower part of the oceanic crust forms by slow crystallization of a magmatic system dominated by

Valentin Basch
valentin.basch@gmail.com

¹ Department of Earth and Environmental Sciences, University of Pavia, Via Ferrata, 1, 27100 Pavia, Italy

² CNR-IGG, Sezione di Pavia, Pavia, Italy

³ Géosciences Montpellier, CNRS, University of Montpellier, Montpellier, France

⁴ Department of Earth, Environmental and Life Sciences, University of Genova, Genoa, Italy

crystal mushes (i.e., crystal-rich magma reservoirs; see Lissenberg et al. 2019).

The evolution of a crystal mush involves multiple processes occurring concomitantly: magma replenishment, mixing, extraction, crystallization, assimilation, compaction, and deformation (e.g., Coogan and Dosso 2016; O'Neill and Jenner 2016; Cashman et al. 2017; Edmonds et al. 2019; Boulanger et al. 2020; Basch et al. 2023). Yet, the overarching characteristic of crystal mushes is that melt migration mainly occurs by porous flow of melts through a crystal-dominated matrix (Leuthold et al. 2018; Lissenberg et al. 2019; Zhang et al. 2020; Boulanger et al. 2021; Ferrando et al. 2021a, b), rather than by episodic and focused melt extraction. Such diffuse migration of melts through a pre-existing matrix has strong implications on the chemical and structural evolution of the crystallizing lithologies; it favours reactive processes that impact on the compositional evolution of melt (e.g., Lissenberg et al. 2013; Leuthold et al. 2018; Sanfilippo et al. 2020; Ferrando et al. 2021a), and possibly drives the development of flow-induced fabrics within lower crustal gabbroic lithologies (Cheadle and Gee 2017; Lissenberg et al. 2019; Ferrando et al. 2021b). However, the role of the instantaneous melt/rock ratio (i.e., the porosity of the magmatic system) or melt/rock ratio integrated over time (i.e., the total amount of melt involved in the reactive percolation over time) in the structural and chemical evolution of crystal mush systems is not well constrained yet.

Here, we combine microstructural and in situ geochemical data to highlight the control of melt flow and distribution on the structural and chemical evolution of the base of the crustal section—the Moho Transition Zone—atop the Maqsad mantle diapir in the Oman ophiolite. The Moho Transition Zone is characterized by a compositional layering of dunite, troctolite and gabbroic rocks. Previous studies argued that this layering formed during reactive melt migration processes that led to progressive impregnation and hybridization of a dunitic protolith into gabbroic lithologies (e.g., Boudier and Nicolas 1995; Dijkstra et al. 2002; Higgie and Tommasi 2012; Jousset et al. 2021). At the Moho Transition Zone, deformation-controlled melt distribution created a centimetre-size layering between mildly impregnated dunites and strongly percolated and hybridized olivine gabbros (Higgie and Tommasi 2012), thus providing an ideal setting to document the evolution of textures and mineral chemical compositions during diffuse and focused percolation. Combining our new dataset with geochemical models, we investigate the linkage between deformation, reactive melt flow, and their contribution to incipient layering and magma transport at the mantle/crust interface beneath a fast-spreading ridge.

Geological setting of the Maqsad Moho transition zone

The Oman ophiolite is among the best preserved outcropping section of fossil oceanic lithosphere in the world (e.g., Browning 1984; Boudier and Nicolas 1985; Boudier et al. 1996). It is composed of a thick stratified oceanic crustal sequence, recording the presence of long-lived magma chambers in a former fast-spreading ridge environment (e.g., Nicolas and Boudier 1995; Boudier et al. 1997; Grambling et al. 2022). High-resolution dating constrained the half-spreading rate of the Oman lithosphere to be ~10 centimetres/year (Rioux et al. 2012, 2013), similar to present-day East Pacific Rise (Toomey et al. 2007; Müller et al. 2008).

Throughout the Oman ophiolite, differences in melt composition of different magmatic events reflect a progressive evolution in the geodynamic setting of the Oman ophiolite, from decompressional melting-related crustal accretion to an increased “arc signature”, mostly evident in the northern massifs (e.g., Godard et al. 2003; Goodenough et al. 2014; Belgrano and Diamond 2019; Guilmette et al. 2021). Namely, two main magmatic suites have been distinguished in the extrusive and intrusive sections (e.g., Einaudi et al. 2003; Godard et al. 2003; Belgrano et al. 2019). The N-MORB-type V1 magmatism is exposed ubiquitously along the Oman ophiolitic massifs and is associated with crustal accretion at the Oman paleo-ridge axis (94–95 Ma; e.g., Belgrano and Diamond 2019 and references therein). On the other hand, V2 magmatism is made of low-Ti tholeiitic melts, depleted in incompatible trace elements, and is interpreted either as the first stages of island arc volcanism in an immature arc environment (Pierce et al. 1981; Beurrier et al. 1989; Godard et al. 2003), or as the product of fluid-enhanced melting during intra-oceanic thrusting of the Oman paleo-ridge (Boudier et al. 1988; Ernewein et al. 1988).

Extensive mapping of mantle flow patterns has been performed within the southern Oman ophiolite (Samail, Wadi Tayin), which best exposes the lithospheric accretion phase (V1 magmatism). This provided evidence of diapiric structures displaying kilometre-scale zones of steeply-dipping peridotite lineations and foliations with radial patterns (Fig. 1) (Nicolas et al. 2000 and references therein). These diapirs are the direct expression of mantle upwelling underneath a ridge axis and are topped by a layer of dunites indicative of large quantities of melt flowing through and accumulating at the mantle-crust transition (Boudier and Nicolas 1995; Godard et al. 2000; Higgie and Tommasi 2012; Abily and Ceuleneer 2013; Rospabé et al. 2018). This layer, located at the top of the mantle sequence (Fig. 1b) and named the Dunitic or Moho Transition Zone (MTZ), represents an important interface controlling melt evolution and

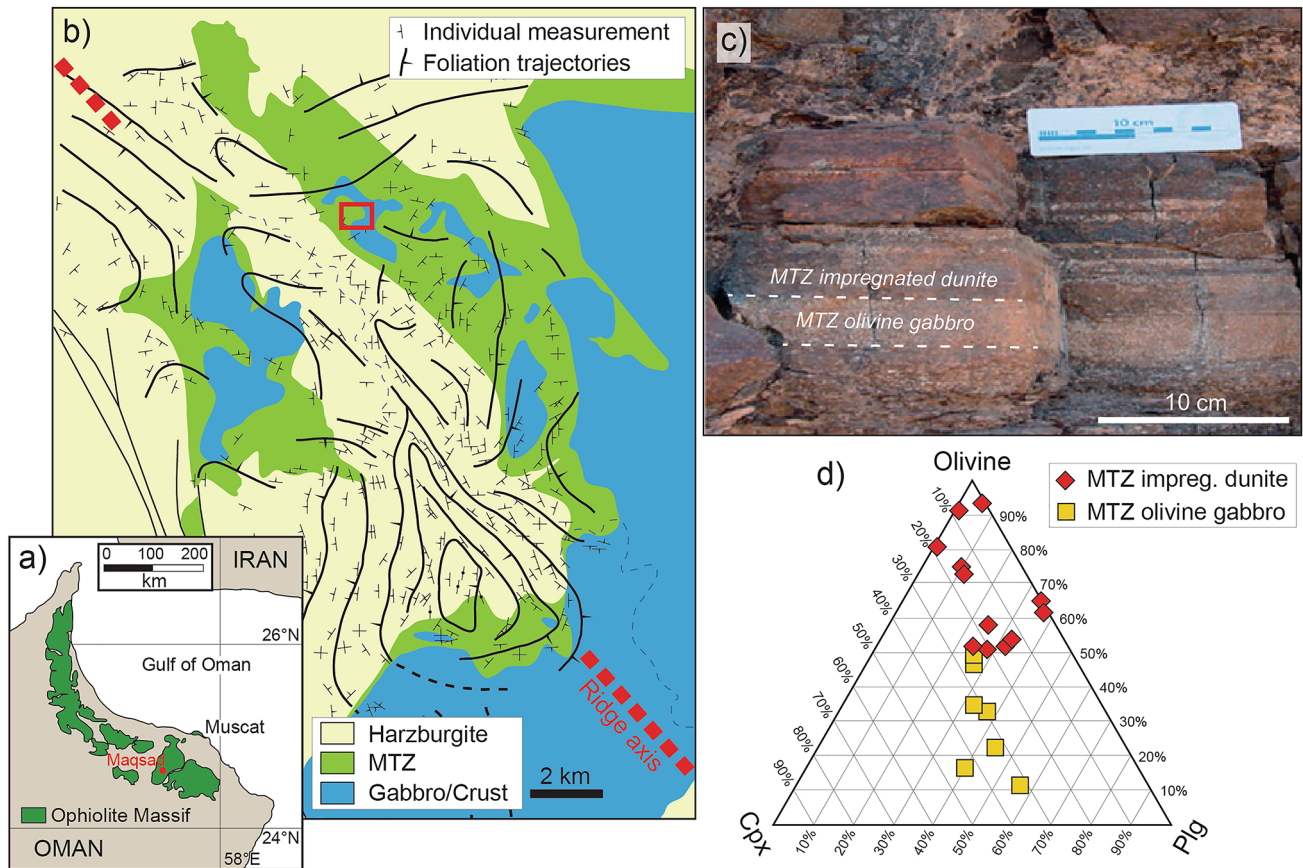


Fig. 1 Geological setting and field occurrences of the studied samples, after Higgle and Tommasi (2012). **a** Map of the Oman ophiolite, locating the Maqсад area; **b** Map showing individual foliation measurements and interpreted foliation trajectories, highlighting the vicinity of the study area (red box) to the Maqсад diapir, and the proposed position of the paleo-ridge axis, redrawn after Joussetin and Mainprice (1998); **c** Photograph of sub-horizontal layering in the central part of the investigated MTZ section with gabbroic lenses (grey, up to 10 cm-

thick) intercalated with thin olivine-rich layers (brown) parallel to foliation; **d** Ternary modal composition diagram of studied samples from the Oman MTZ. Note that sample groups *MTZ impregnated dunite* and *MTZ olivine gabbro* are defined on the basis of olivine modal amount (> 50 vol% and < 50 vol%, respectively) and microstructure (e.g. olivine CPO available by Higgle and Tommasi 2012; see text for further details)

delivery to crustal levels. The origin of this dunitic pile has been previously interpreted either through magmatic accumulation of olivine from Mg-rich melts (e.g., Elthon 1979; Abily and Ceuleneer 2013; Kelemen et al. 2020) or after reactive percolation processes, progressively transforming mantle peridotites into dunites (e.g., Boudier and Nicolas 1995; Kelemen et al. 1995; Rospabé et al. 2018; Joussetin et al. 2021; Klaessens et al. 2021). Notably, regardless of the origin of the dunitic matrix, the investigated melt migration and reactive processes are known to occur in the lowermost crust and subridge mantle (e.g., Lissenberg et al. 2019), and mantle-derived lithologies can be strongly hybridized and incorporated into the crustal sequence (see Joussetin et al. 2012; Ferrando et al. 2020). We thus argue that the formation process of the Oman MTZ dunite has no fundamental implication on the melt migration processes here investigated.

In the Maqсад Massif, the MTZ is a hundred-metre-size unit composed of sub-horizontal interlayered centimetre- to metre-thick dunites, wehrlites, troctolites and olivine gabbros, which separates the lower gabbros from the dominantly harzburgitic mantle (Fig. 1c; e.g., Boudier and Nicolas 1995; Kelemen et al. 1997; Koga et al. 2001; Joussetin et al. 2012; Koepke et al. 2021; Müller et al. 2022; Tamura et al. 2022). The layering is sub-parallel to the foliation (Higgle and Tommasi 2012) and occurs at all scales. Based on detailed petrostructural data, in particular the analysis of the olivine crystal preferred orientation (CPO) in the different layers, several authors (e.g., Boudier and Nicolas 1995; Dijkstra et al. 2002; Higgle and Tommasi 2012) interpreted the MTZ troctolites and olivine gabbros as formed by reactive processes involving focused percolation within pre-existing dunites (whether reactive or cumulitic). According to this interpretation, the layering between MTZ dunites and olivine gabbros resulted from variable amounts of reactive

melt percolation within a dunitic precursor, progressively hybridizing the latter ultramafic lithology into gabbroic rocks.

Studied samples

The studied samples have been recovered from an 80 m-thick continuous section of the 250 m-thick Maqsad MTZ near Tuf (23°07'00"N, 57°56'21"E). We selected 19 olivine-bearing layers, ranging from dunites to troctolites, wehrlites and olivine gabbros. These samples were previously investigated by Higgin and Tommasi (2012), who provided a detailed characterization of their modal content and microstructures (Fig. 2; Supplementary Figures S1, S2). Four of the studied thin sections show modal layering with straight and relatively sharp contacts (Fig. 1d); we considered each compositional layer at the thin section scale as a separate sample (Supplementary Table S1; Supplementary Figure S3). Our rock collection is spread throughout the section and covers the whole lithological and microstructural variability observed in the Maqsad MTZ (Figs. 1c and d and 2; Supplementary Table S1). Based on the previous microstructural study by Higgin and Tommasi (2012) identifying a transition in olivine CPO between 70 and 40 vol%, together with new petrographic and major element chemical features, we redefined the sample division into: Group (1) *MTZ impregnated dunites*, containing more than 50 vol% olivine and less than 25 vol% clinopyroxene, and Group (2) *MTZ olivine gabbros*, containing less than 50 vol% olivine and more than 25 vol% clinopyroxene.

Petrography and microstructure of the selected layers

The *MTZ impregnated dunite* samples (Group 1) comprise 2 dunites, 2 troctolites, 1 wehrlite and 8 olivine gabbros (Fig. 1d). All *MTZ impregnated dunites* are composed of abundant modal olivine and variable proportions of clinopyroxene and plagioclase (Fig. 2a, b; Supplementary Table S1). Spinel locally forms trails parallel to the olivine foliation in the most olivine-rich samples (Fig. 2a); the latter dunitic samples commonly exhibit larger proportions of clinopyroxene than plagioclase (Fig. 1d). Olivine mainly occurs as millimetre-size grains showing lobate contacts with clinopyroxene and plagioclase (Fig. 3a, b,c), and in places as 100 μm -size rounded olivine chadacrysts included in interstitial clinopyroxene and plagioclase (Fig. 3b, c). Olivine forms a foliation of slightly elongated and deformed crystals (aspect ratios 2:1; Fig. 3a, b,c), with common occurrence of subgrain boundaries normal to the

crystal elongation. With decreasing modal contents, olivine tends to decrease in grain size and form an irregular and discontinuous “network” of elongated crystals, which progressively display more irregular shapes (Fig. 3b, c). In the *MTZ impregnated dunite* samples, olivine CPO is characterized by a strong to moderate axial-[100] crystallographic preferred orientation (Fig. 2a, b; data from Higgin and Tommasi 2012). The fabric strength, quantified by the J-index, ranges from 3 to 6.5 and the BA-index, which quantifies the symmetry of the CPO (i.e., 0 for axial-[010] and 1 for axial-[100]; see Mainprice et al. 2014), varies from 0.5 to 0.9 and slightly decreases with decreasing olivine modal contents (Supplementary Figure S1). Clinopyroxene and plagioclase occur mainly as irregularly shaped crystals slightly elongated parallel to the foliation, but rounded crystals are locally observed (Figs. 2b and 3a, b and c). In contrast with olivine, plagioclase and clinopyroxene display no evidence for intracrystalline deformation.

The *MTZ olivine gabbros* (Group 2) include 6 olivine gabbros *sensu stricto* (Fig. 1d; Supplementary Table S1). *MTZ olivine gabbros* are distinguished from *MTZ impregnated dunites* by a marked foliation defined by smaller and elongated olivine crystals (aspect ratio > 3:1) and a weak shape-preferred orientation of plagioclase and clinopyroxene (Fig. 2d). This foliation is parallel to the modal layering observed in some samples at the scale of the thin section. At decreasing olivine modal contents, olivine crystals show increasingly irregular and cusped grain boundaries at the contact with plagioclase and clinopyroxene (Fig. 3d, e,f). Subgrain boundaries in olivine crystals are rarer than in *MTZ impregnated dunites* but are locally observed. In the most olivine-poor samples (~ 5–10 vol% olivine), fine-grained olivine crystals (100–300 μm) are embedded in a plagioclase and clinopyroxene matrix with interstitial to poikilitic habitus (Fig. 3e, f). When compared to *MTZ impregnated dunites*, olivine CPO has similar to slightly weaker intensities (J-index = 3–5) of axial-[010] patterns (Fig. 2c, d), with BA-index ranging from 0.2 to 0.4 (data from Higgin and Tommasi 2012). Similar to Group 1 samples, plagioclase and clinopyroxene forming Group 2 *MTZ olivine gabbros* display no evidence for intracrystalline deformation.

Analytical methods

We performed major and trace element analyses of olivine, plagioclase and clinopyroxene (Supplementary Table S1) from 8 layers: 4 *MTZ impregnated dunite* layers (1 dunite and 3 olivine gabbro *sensu stricto*) and 4 *MTZ olivine gabbros* layers (4 olivine gabbros *sensu stricto*).

Major element compositions (SiO_2 , TiO_2 , Al_2O_3 , Cr_2O_3 , FeO , MgO , MnO , CaO , NiO , Na_2O and K_2O) were analysed

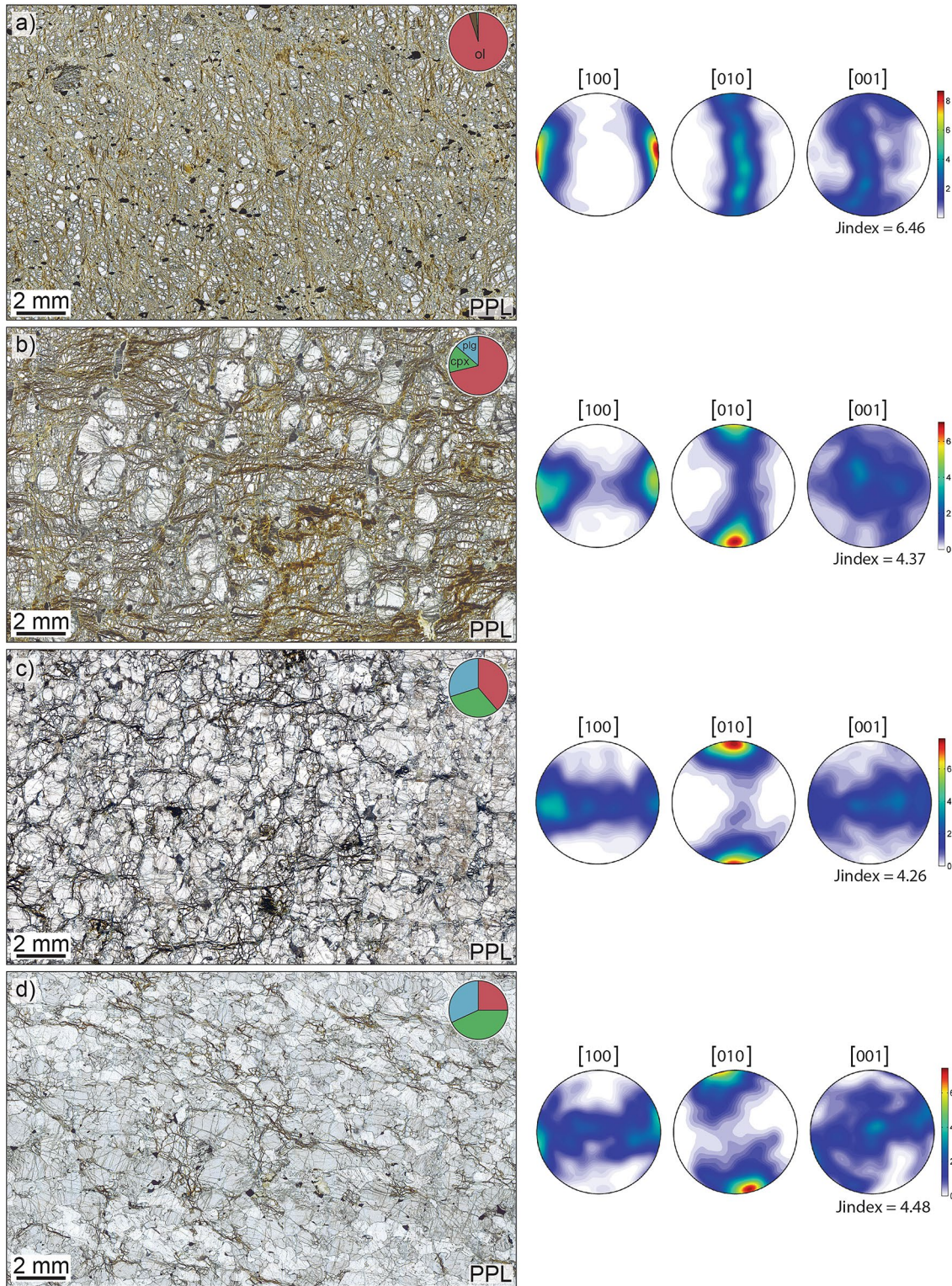


Fig. 2 Plain-polarized thin section photomicrograph and associated olivine CPO of representative samples of *MTZ impregnated dunite* (Group 1, **a, a**) and *MTZ olivine gabbro* (Group 2, **c, d**). **a** Dunite characterized by a strong axial-[100] olivine CPO; **b** Olivine-rich gab-

bro characterized by a moderate axial-[100] olivine CPO; **c**) Olivine gabbro characterized by an axial-[010] olivine CPO; **d**) Olivine gabbro characterized by an axial-[010] olivine CPO. Microstructural data are after Higgie and Tommasi (2012)

Group 1 - MTZ impregnated dunite

Group 2 - MTZ olivine gabbro

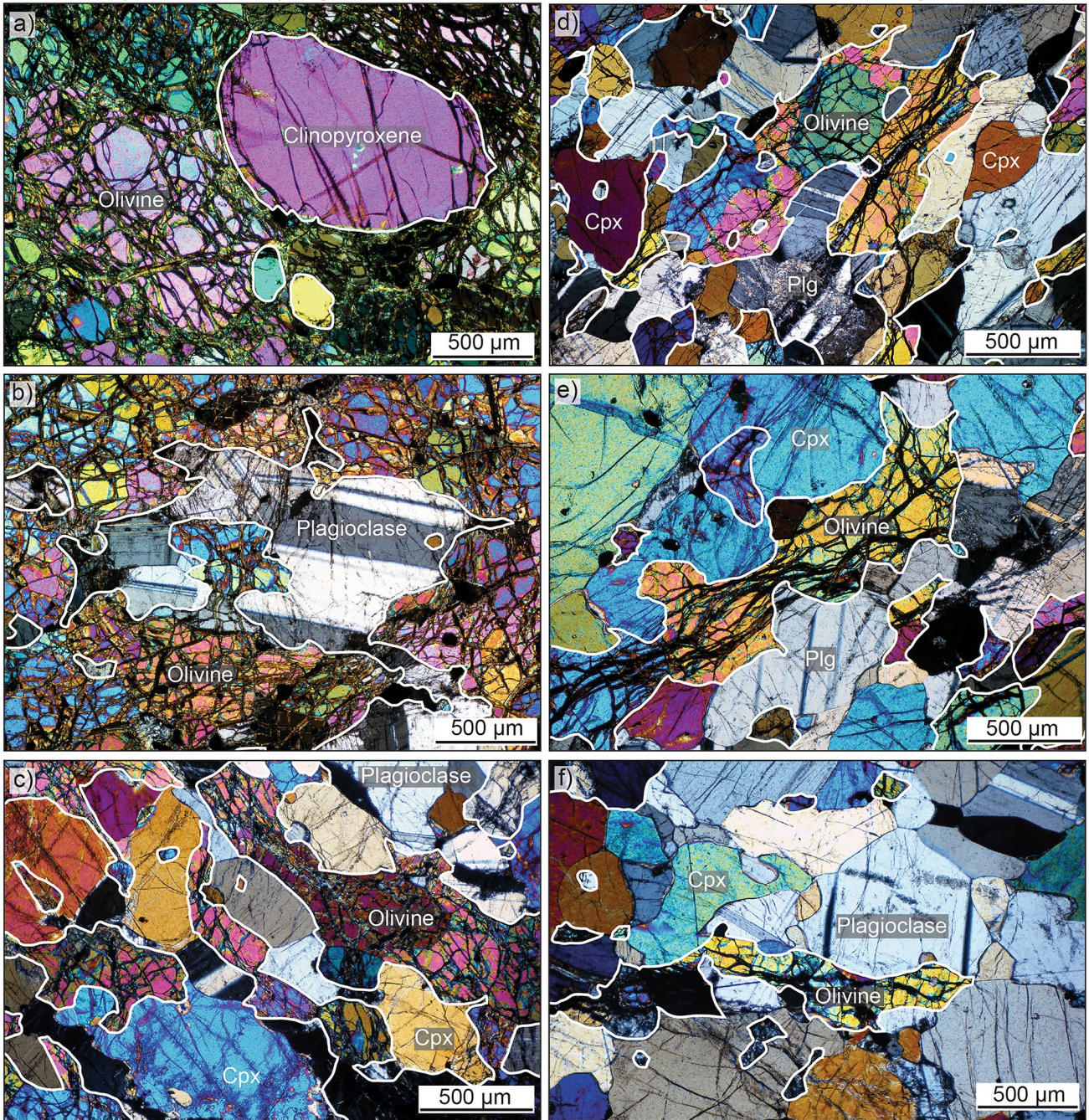


Fig. 3 Representative crossed-nicols (XPL) photomicrographs. White contours outline the contact between olivine and interstitial minerals; a) MTZ impregnated dunite 100K27, showing an millimetre-size undeformed clinopyroxene crystal developing embayments on the olivine matrix; b) MTZ impregnated dunite 100K34B, showing interstitial to poikilitic plagioclase developing embayments on olivine crystals; c) MTZ impregnated dunite 100K35, illustrating the development of an irregular network of elongated olivine crystals; d) MTZ olivine gabbro, 100K25A-2, showing widespread embayments

of interstitial to poikilitic plagioclase and clinopyroxene onto olivine irregular network; e) MTZ olivine gabbro 100K25A-1 showing development of cusped grain boundaries of olivine after extensive dissolution and formation of interstitial plagioclase and clinopyroxene; (f) MTZ olivine gabbro 100K16A evidencing the disaggregation of olivine crystals characterized by common extinction. Both clinopyroxene and plagioclase include 100–300 μm olivine chadacrysts

at the Dipartimento di Scienze della Terra, University of Milano using a JEOL JXA 8200 Superprobe equipped with five wavelength-dispersive (WDS) spectrometers, an energy dispersive (EDS) spectrometer, and a cathodoluminescence detector (with accelerating potential 15 kV, beam current 15 nA). The analyses of all elements and phases were performed with a beam size of 3 μm ; different peak and background time of analysis have been used for each element, depending on the analysed phase, to maximize accuracy and sensitivity. Analyses with total oxide percentage lower than 98%, and higher than 102% were excluded. A mixture of natural and synthetic minerals and oxides were used as standards. Furthermore, the quality of analyses was assessed on the basis of the atom per formula units and by repeated analyses of San Carlos olivine and Kakanui augite as external standards (Jarosewich et al. 1980).

In-situ trace element compositions were determined at Géosciences Montpellier by Laser Ablation-Inductively Coupled Plasma Mass Spectrometry (AETE-ISO facility, University of Montpellier, France). Analyses were performed with a Thermo Scientific Element XR (eXtended Range) high resolution ICP-MS, coupled to a laser ablation system consisting of a Geolas (Microlas) automated platform with a 193 nm Excimer Compex 102 laser from Lambda Physik. The laser energy density was set to 12 $\text{J}\cdot\text{cm}^{-2}$ at a frequency of 8 Hz and the laser spot size was set to 100 μm , for an ablation time of one minute. NIST 612 was analysed as internal standard, and the acquired data were processed with GLITTER (Van Achterberg et al. 2001), filtered for spikes, using ^{29}Si for the standardization for all minerals. Mean detection limits were < 7 ppb for Rb, Sr, Y, Zr, Nb, Sb, Ba, REE, Hf, Ta, Pb, Th, U, < 70 ppb for Zn, Cu, Co, Mn, V, Sc, < 170 ppb for Li and B and < 1 ppm for Ti, Cr and Ni. Values that were within 1σ of the detection limit were excluded during data reduction. Sensitivities were > 300 cps/ppm for Ni and Ti, > 1000 cps/ppm for B and Zn, 1000–5000 cps/ppm for Li, Cr, Cu, Ba, Nd, Sm, Gd, Dy, Er, Yb and Hf and > 5000 cps/ppm for all other elements. Reproducibility and accuracy have been constrained by 14 analyses of reference basalt BIR 1-G as an external standard (Supplementary Table S1). Reproducibility was better than 10% for all elements except Li, (10.4%), Gd (10.8%), Tm (10.7%), Hf (11.0%), Th (12.2%), and measured values were comparable within analytical uncertainties to GEO-REM accepted values (Jochum et al. 2005).

Results

Mineral major and minor element compositions

Olivine shows a strong variability of forsterite content ($\text{Fo} = \text{Mg}/[\text{Mg} + \text{Fe}]$ mol%), with the highest values in the *MTZ impregnated dunites* ($\text{Fo} = 87.1\text{--}89.0$ mol%) and the lowest in the *MTZ olivine gabbros* ($\text{Fo} = 82.7\text{--}84.9$ mol%). Notably, *Group 1* and *Group 2* samples are characterized by two distinct and narrow compositional ranges (Figs. 4 and 5) despite their drastic variability in olivine modal contents (from 93 vol% to 12 vol%). Mn and Ni display negative and positive correlations with Forsterite contents, respectively. *MTZ impregnated dunites* show high Ni (1450–2651 ppm) and low Mn contents (1447–1693 ppm) compared to *MTZ olivine gabbros* (Ni = 1179–1625 ppm; Mn = 1778–2052 ppm) (Fig. 5a, b). In the *MTZ olivine gabbros*, olivine does not show any core-to-rim zonation associated with dissolution textures (Supplementary Figure S4). The high Ni and Forsterite contents of some of the *MTZ impregnated dunites* are comparable to olivine compositions in spinel peridotites from the Oman ophiolite mantle section (Fig. 5b; e.g., Hanghoj et al. 2010; Rospabé et al. 2018). Overall, the analysed olivine chemical composition cover the compositional field previously reported for the Oman MTZ (Fig. 5a, b; Korenaga and Kelemen 1997; Rospabé et al. 2018).

Clinopyroxene Mg-numbers ($\text{Mg\#} = \text{Mg}/[\text{Mg} + \text{Fe}] \times 100$ mol%) are positively correlated with the olivine Fo content and follow Fe-Mg equilibrium between olivine and clinopyroxene (Supplementary Figure S5, e.g., Lissenberg and Dick 2008). *MTZ impregnated dunites* are characterized by high clinopyroxene Mg-numbers ($\text{Mg\#} = 87.9\text{--}90.8$ mol%) and Cr_2O_3 contents ($\text{Cr}_2\text{O}_3 = 0.94\text{--}1.38$ wt%), whereas the *MTZ olivine gabbros* show lower Mg-numbers and Cr_2O_3 contents ($\text{Mg\#} = 84.9\text{--}89.0$ mol%, $\text{Cr}_2\text{O}_3 = 0.25\text{--}0.64$ wt%) (Fig. 5c). Similar to olivine, clinopyroxenes do not define a continuous trend of chemical variation but rather define two distinct compositional fields (Fig. 5c). Clinopyroxene compositions within *MTZ olivine gabbros* are similar to clinopyroxenes previously reported in the Oman MTZ (Korenaga and Kelemen 1997; Koga et al. 2001), and show slightly more primitive compositions with respect to the Oman lower crustal gabbros (i.e., Müller et al. 2022; VanTongeren et al. 2022), with higher Mg-numbers and Cr_2O_3 contents (Fig. 5c; Supplementary Figure S5).

Plagioclase is characterized by a wide range of Anorthite contents ($\text{An} = \text{Ca}/[\text{Ca} + \text{Na} + \text{K}]$ mol%) (Fig. 6). Within the *MTZ impregnated dunite* samples, Anorthite content is negatively correlated with olivine modal contents, showing lower and more variable An (82.6–86.2 mol%) in the dunites *sensu stricto* and increasing An contents (89.1–92.3 mol%) with decreasing olivine modal amount. Plagioclase within

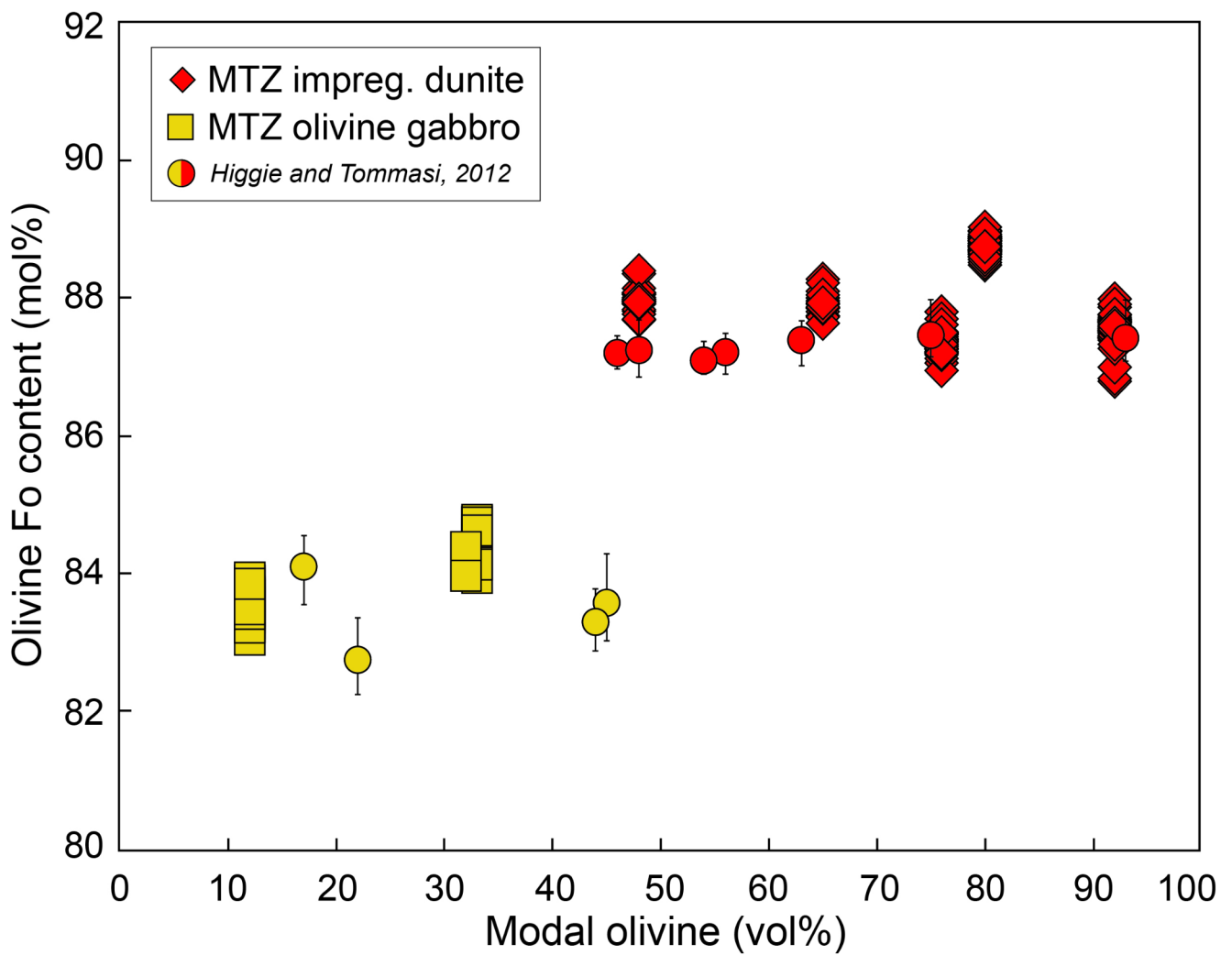


Fig. 4 Modal composition of olivine within the studied samples vs. olivine forsterite content ($Fo = Mg/[Mg + Fe]$ mol%). Error bars for samples from Higgin and Tommasi (2012) correspond to the standard deviation of the olivine Fo content

the *MTZ olivine gabbro* samples show more homogeneous Anorthite contents ($An = 87.1\text{--}92.5$ mol%), similar to *MTZ impregnated dunites* having the lowest olivine abundances (50–65 vol%). Notably, in the $Forsterite_{ol}$ - $Anorthite_{plg}$ space, these compositions define two distinct trends; *MTZ impregnated dunites* show variability in Anorthite contents at relatively constant Forsterite values, whereas *MTZ olivine gabbros* show a positive correlation between olivine and plagioclase compositions, at relatively lower Forsterite and high Anorthite contents (Fig. 6). Plagioclase compositions are similar to those previously reported in the Oman MTZ (Korenaga and Kelemen 1997; Koga et al. 2001) and show slightly higher Anorthite contents respect to the Oman lower gabbroic crust (Browning 1982; Müller et al. 2022; VanTongeren et al. 2022).

Mineral trace element compositions

Olivine is characterized by low abundances of incompatible trace elements and a strong decrease in concentration from Heavy (H-) to Middle (M-) Rare Earth Elements (REE) (Fig. 7a). Olivine from the *MTZ impregnated dunite* samples show higher and more variable H-REE and M-REE concentrations ($Yb_N = 0.023\text{--}0.077$, $N = PM$ -normalized, after Sun and McDonough 1989) than olivine in *MTZ olivine gabbros* ($Yb_N = 0.015\text{--}0.022$). In *MTZ impregnated dunite* samples, the highest HREE concentrations are measured in samples having the highest olivine fraction (Supplementary Table S1). The compositions of olivines within the Maqsad MTZ are intermediate between the compositional fields of replacive olivine-rich troctolites from Atlantis Massif (Mid-Atlantic Ridge; Drouin et al. 2009; Ferrando et al. 2018) and Erro-Tobbio ophiolite (Ligurian Alps; Rampone et al. 2016;

Fig. 5 Forsterite content in olivine vs. **a** Mn (ppm) and **b** Ni (ppm) and **c** Cr_2O_3 (wt%) in associated clinopyroxene. The investigated samples are compared to Oman lower crustal gabbros after Browning (1982), Müller et al. (2022) and VanTongeren et al. (2022), and Oman Moho Transition Zone from Korenaga and Kelemen (1997) and Rospabé et al. (2018)

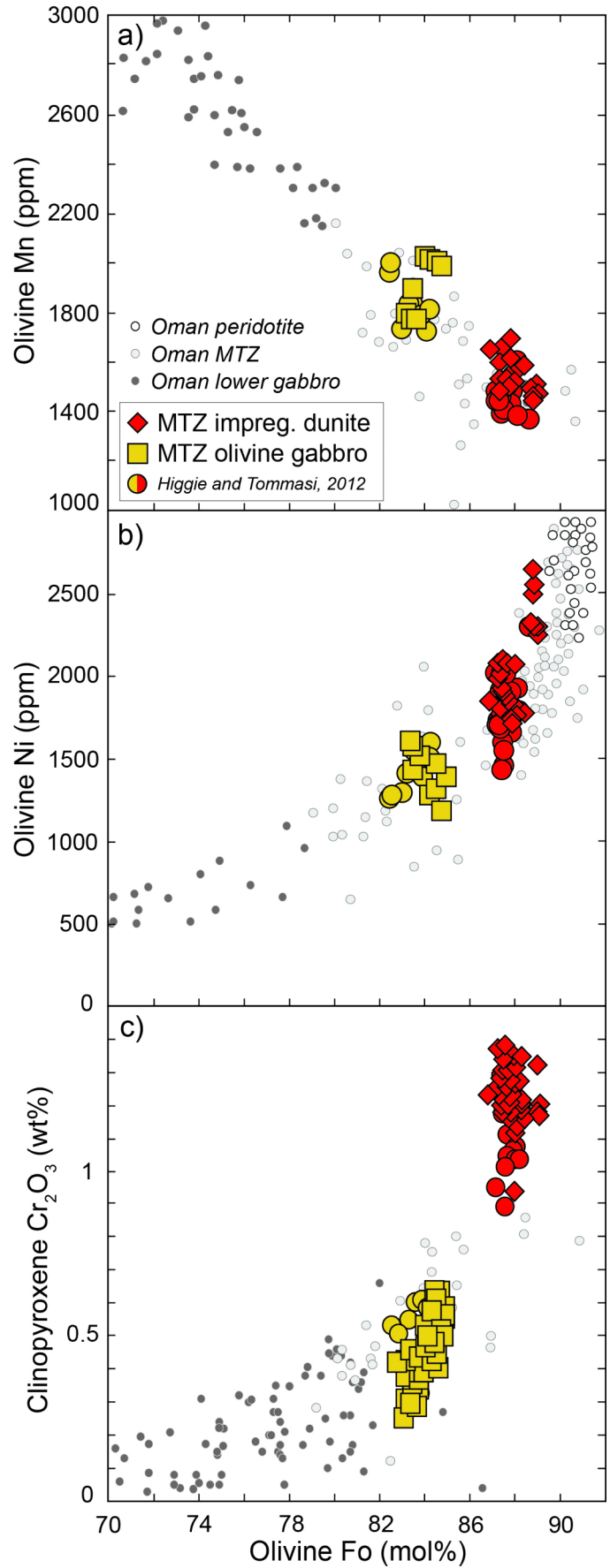
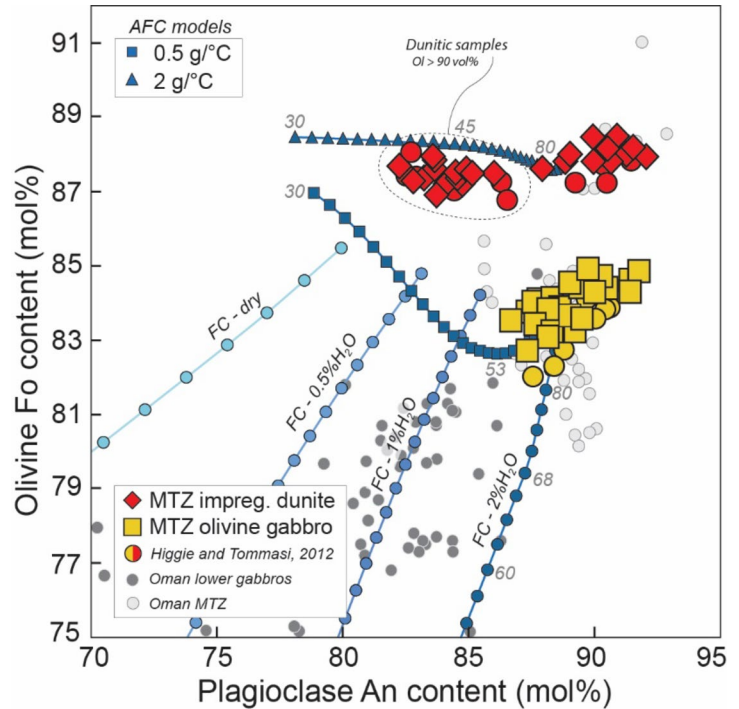


Fig. 6 Anorthite content (mol%) in plagioclase vs. forsterite content (mol%) in olivine. Oman lower crustal gabbros (Browning 1982; Müller et al. 2022; VanTongeren et al. 2022) and Moho Transition Zone gabbros (Korenaga and Kelemen 1997; Koga et al. 2001) are shown for comparison. Also shown are models of dry and hydrous (0.5–2 wt% H₂O) fractional crystallization of a tholeiitic melt (AH6 after Husen et al. 2016) computed using Rhyolite-MELTS v1.2 (Ghiorso and Gualda 2015), and models of assimilation-fractional crystallization (AFC) involving the assimilation of 0.5 to 2 g of olivine Fo_{88.8} (dunite composition) for each degree of cooling of the hydrous melt. Each symbol along the modeled trends correspond to 5 °C cooling interval. Grey italic numbers near the modeled trends indicate the computed remaining proportion of melt



Basch et al. 2021), and mantle-derived olivines (Demouchy and Alard 2021).

Clinopyroxene trace element compositions in *MTZ impregnated dunite* and *MTZ olivine gabbro* samples mostly overlap and are comparable to those of clinopyroxenes previously reported in MTZ gabbros (Kelemen et al. 1997; Koga et al. 2001) and in the most trace element depleted lower crustal gabbros (Kelemen et al. 1997; Müller et al. 2022). They are characterized by almost flat Heavy to Middle-REE and depleted Light (L-) REE on PM-normalized trace element patterns (Fig. 7b). In *MTZ impregnated dunite* samples, clinopyroxene shows slightly higher and more variable H-REE concentrations ($Yb_N = 1.48\text{--}2.33$) relative to clinopyroxene in *MTZ olivine gabbros* ($Yb_N = 1.19\text{--}1.82$). L-REE/H-REE ratios are low in both *MTZ impregnated dunites* ($Ce_N/Yb_N = 0.11\text{--}0.23$) and *MTZ olivine gabbros* ($Ce_N/Yb_N = 0.14\text{--}0.16$). Zr and Hf show negative anomalies relative to neighbouring elements in all samples, with Zr characterized by stronger depletion than Hf. Clinopyroxene within *MTZ impregnated dunite* samples are also distinguished by negative anomaly of Sr ($Sr/Sr^* = 0.48\text{--}0.86$), whereas the *MTZ olivine gabbros* are characterized by positive anomalies ($Sr/Sr^* = 1.14\text{--}2.08$) (Fig. 7b).

Plagioclase is characterized by relatively homogeneous compositions of incompatible trace elements in *MTZ impregnated dunite* and *MTZ olivine gabbro* samples (Fig. 7c), overlapping with compositions reported for MTZ gabbros (Kelemen et al. 1997; Koga et al. 2001; Nicolle et al. 2016) and slightly more trace element-depleted than those analysed in Oman lower crustal gabbros (Müller et al.

2022). PM-normalized trace element patterns show decreasing concentrations from L-REE to H-REE, with strong positive anomalies in Eu and Sr, and negative anomalies of Zr respect to neighbouring Nd in all samples (Fig. 7c). Plagioclase shows low L-REE contents and L-REE/M-REE ratios in *MTZ impregnated dunite* samples ($Ce_N = 0.05\text{--}0.11$, $Ce_N/Sm_N = 1.19\text{--}2.05$) and *MTZ olivine gabbros* ($Ce_N = 0.05\text{--}0.08$, $Ce_N/Sm_N = 0.72\text{--}2.39$).

Discussion

Formation of the Moho Transition Zone layering

The Moho Transition Zone is located at the base of the oceanic crustal sequence and is thought to exert a certain control on the chemical evolution of melts feeding the spreading ridge (e.g., Einaudi et al. 2003; Abily and Ceuleneer 2013). Yet, better constraints on melt transport processes are required in our global understanding of the ridge system. In the Maqсад Massif MTZ, decreasing olivine modal contents within *MTZ impregnated dunites* and *MTZ olivine gabbros* are correlated with a progressive decrease in olivine grain size and an increase in textural irregularity and dissolution features (Fig. 3; Higgle and Tommasi 2012). These microstructures are associated with a modification of the olivine CPO, from axial-[100] to axial-[010] symmetry, the latter microstructure being indicative of the presence of melt during deformation of the olivine matrix (e.g., Holtzman et al. 2003; Le Roux et al. 2008). Higgle

Fig. 7 Primitive Mantle-normalized trace element compositions of: **a** olivine (average per sample), compared with compositional fields of olivines analysed in replacive olivine-rich troctolites (Drouin et al. 2009; Rampone et al. 2016; Ferrando et al. 2018; Basch et al. 2021) and mantle-derived lithologies (Demouchy and Alard 2021); **b** clinopyroxene (single analyses), and **c** plagioclase (single analyses), compared with compositional fields representing clinopyroxene and plagioclase compositions in Moho Transition Zone gabbroic sills (Kelemen et al. 1997; Koga et al. 2001; Nicolle et al. 2016) and lower crustal gabbros (Kelemen et al. 1997; Müller et al. 2022). Normalisation values are after Sun and McDonough (1989)

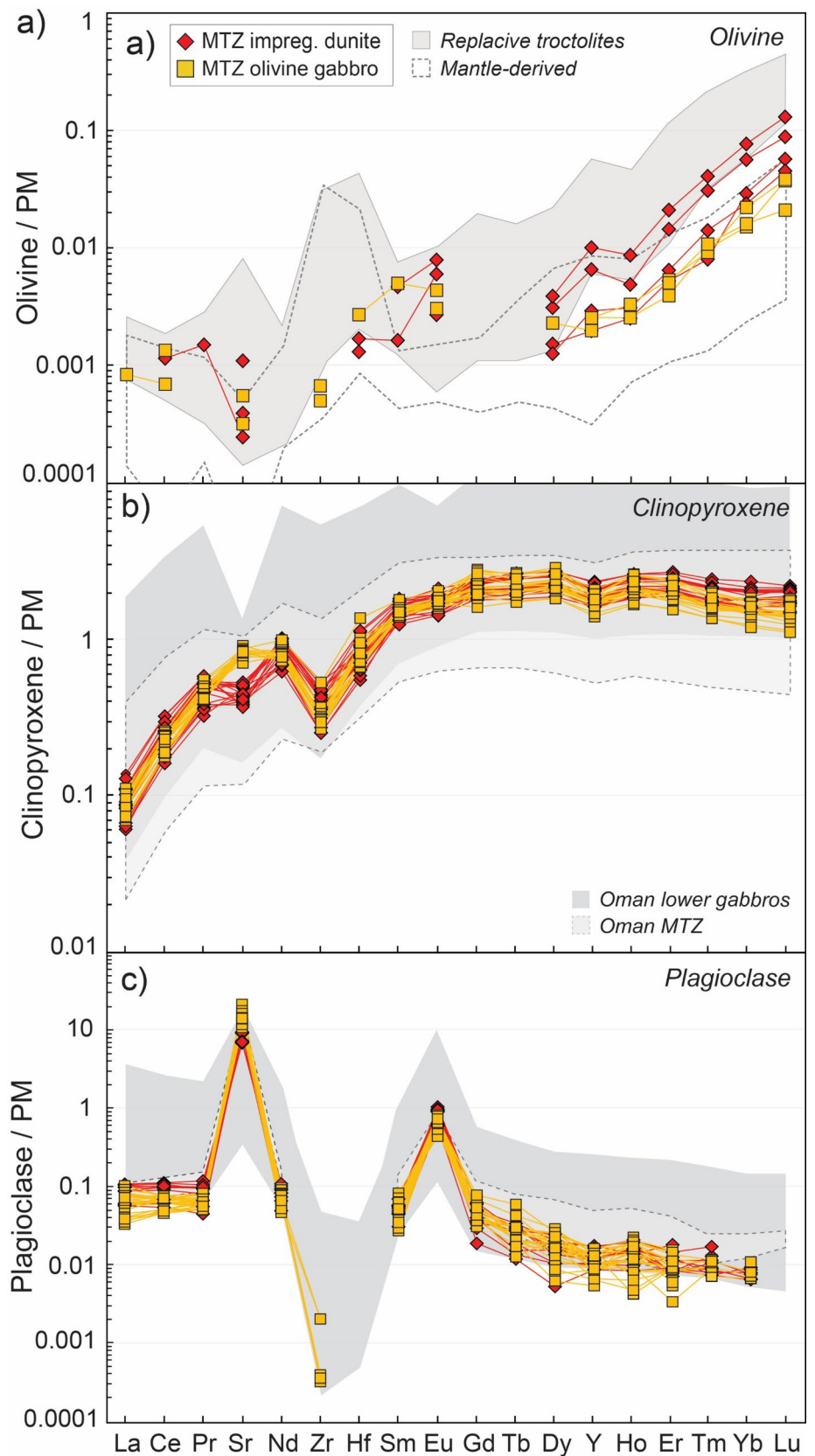
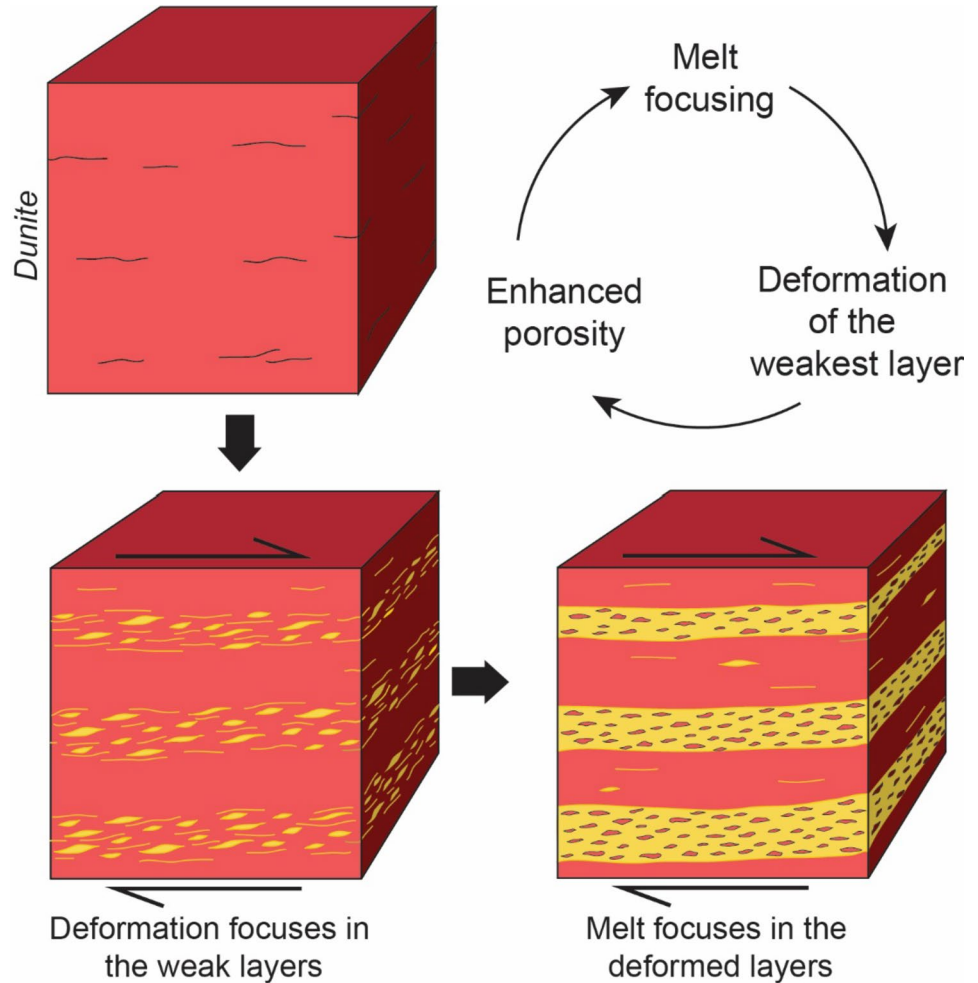


Fig. 8 Representative sketch of the formation process of the MTZ dunite-olivine gabbro layering. Positive feedback between melt focusing and deformation leads to focused percolation within actively deforming layers, allowing for the progressive replacive formation of olivine gabbros

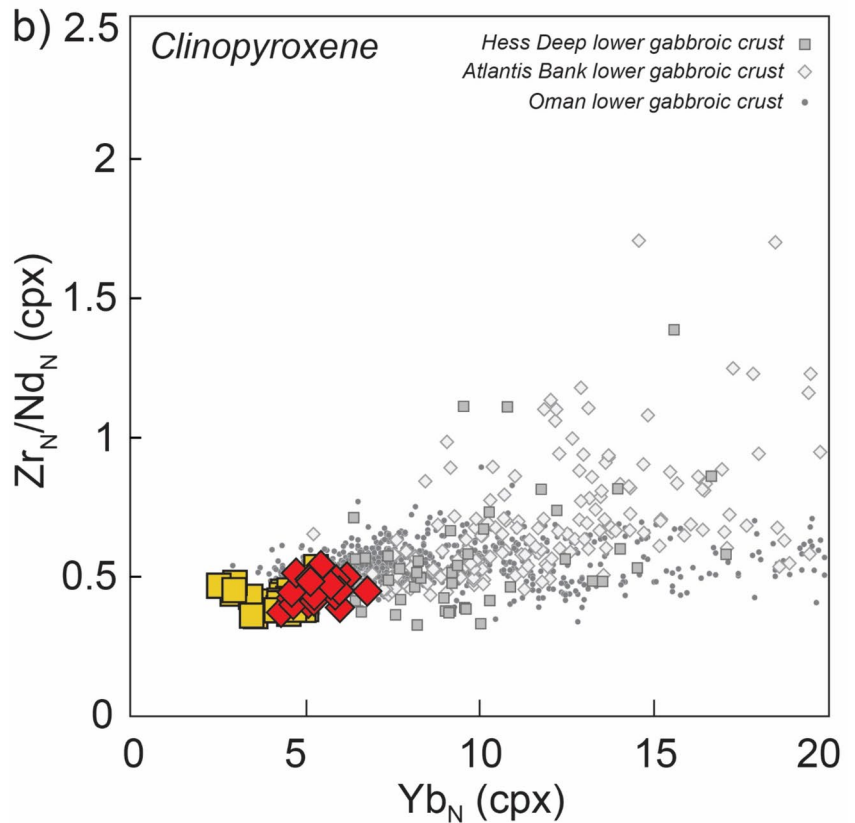
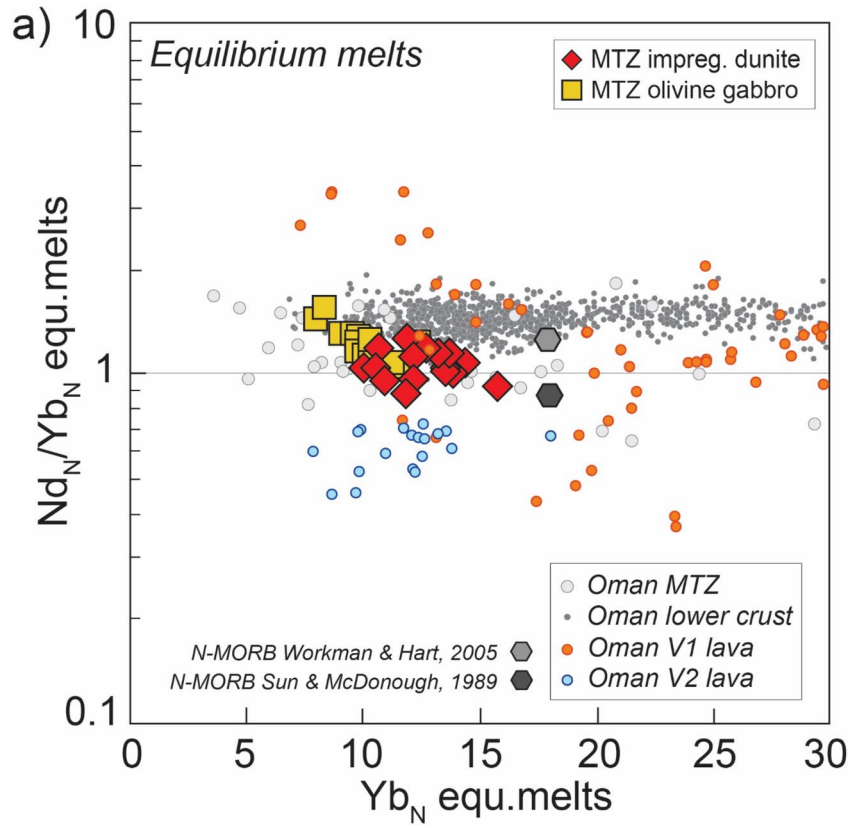


and Tommasi (2012) interpreted this evolution as driven by a positive feedback between deformation and melt distribution, leading to focused percolation within the actively deforming layers (Fig. 8) and continuous reaction between the dunitic matrix and melts. They posit that this reactive process ultimately led to the formation of olivine gabbros containing as low as ~ 10 vol% olivine in the most percolated layers. However, early petrological and geochemical studies of the MTZ from the Maqсад massif had interpreted these gabbroic layers as sills within the crust-mantle transition zone (e.g., Kelemen et al. 1997; Korenaga and Kelemen 1997; Koga et al. 2001; Jousset et al. 2012). Thereafter, we review the petrological and geochemical criteria providing insights on the magmatic processes that drive the development of the MTZ layering.

Considering the complex evolution of the geodynamic setting and magmatism recorded in the Oman ophiolite (e.g., Belgrano and Diamond 2019 and references within), the assessment of the magmatic processes at play and associated compositional evolution first require constraining the geochemical composition of melts infiltrating the Maqсад MTZ layers. We calculated the composition of melts in

equilibrium with clinopyroxene cores, using the compilation of partition coefficients given in Warren (2016). Computed melts show primitive geochemical signature, with low Yb_N concentrations and M-REE/H-REE fractionation similar to N-MORB melts (Sun and McDonough 1989; Workman and Hart 2005) and most V1 lavas (Fig. 9a; Einaudi et al. 2003; Godard et al. 2003), in agreement with previous studies of the Maqсад MTZ (e.g., Koga et al. 2001). These equilibrium melts are also similar but slightly more primitive (i.e., lower Yb_N contents) than parental melts to the lower gabbroic crust (Fig. 9a; clinopyroxene data after Müller et al. 2022). Consistently, clinopyroxenes in the studied samples show MORB-type trace element compositions, characterized by low Yb_N contents and Zr_N/Nd_N plotting at the most primitive end of the compositional field defined by lower oceanic gabbros from both fast- and slow-spreading ridges (Fig. 9b; Wadi Gideah, Oman: Müller et al. 2022; Hess Deep: Basch et al. 2024; Atlantis Bank: Ferrando et al. 2021a). Moreover, their likeness with the trace element composition of clinopyroxenes in the Oman lower crustal gabbros (Fig. 7b) suggests that the melts that formed the layered MTZ percolated upwards to form the lower crustal gabbroic sequence

Fig. 9 Trace element composition of clinopyroxene and melts in equilibrium with clinopyroxene (compilation of partition coefficients after Warren 2016); **a** CI-normalized Yb_N vs. Nd_N/Yb_N ratios of melts in equilibrium with clinopyroxene, compared with N-MORB composition (Sun and McDonough 1989; Workman and Hart 2005), the Oman Moho Transition Zone (Koga et al. 2001; Nicolle et al. 2016), Oman lower gabbroic crust (Müller et al. 2022) and Oman V1 and V2 lavas (Einaudi et al. 2003; Godard et al. 2003); **b** CI-normalized clinopyroxene Yb_N vs. Zr_N/Nd_N , compared with clinopyroxene compositions from the lower gabbroic crust from Oman (Wadi Gideah; Müller et al. 2022), Hess Deep lower gabbroic crust (East Pacific Rise; Basch et al. 2024) and Atlantis Bank lower gabbroic crust (Southwest Indian Ridge; Ferrando et al. 2021a)



(Kelemen et al. 1997; Koga et al. 2001). This in turn indicates that the formation of the layered MTZ is associated with the V1 lithospheric accretion stage.

The similarity between the trace element patterns of the interstitial phases from *MTZ impregnated dunites* and *MTZ olivine gabbros* (i.e., clinopyroxene and plagioclase; Fig. 7b, c) further indicates that a single parental melt was responsible for the formation of all the layers. The parental melts of all clinopyroxenes were more trace element-depleted than a primitive N-MORB (Fig. 9a; N-MORB composition after Workman and Hart 2005). Such systematic primitive character of the parental melt, regardless of the considered lithotype and modal composition, calls for limited fractionation of the melt upon migration through the Maqsad MTZ. This suggests an iterative process of constant extraction of the fractionated melt and replenishment of primitive melt, i.e., a process of continuous melt injection and percolation (see “melt flush process” in Boulanger and France 2023).

The *MTZ impregnated dunites* and *MTZ olivine gabbros* show two distinct and homogeneous compositional ranges of olivine modes and Forsterite contents (Fig. 4), as opposed with the correlation resulting from fractional crystallization processes (e.g., Villiger et al. 2007; Miller et al. 2009; Husen et al. 2016). Namely, the covariation of olivine Forsterite and plagioclase Anorthite contents is expected to define a positive correlation upon progressive fractionation of the melt; within the *MTZ impregnated dunites* and *MTZ olivine gabbros*, mineral compositions do not follow the modeled crystal lines of descent for fractional crystallization of tholeiitic melts (see Fig. 6 for detail), but rather display two distinct chemical trends of evolution between the two sample groups (Fig. 5). Furthermore, mineral trace element contents are expected to increase during progressive melt fractionation, from the most primitive (i.e., dunite, troctolite) to more evolved lithotypes (i.e., olivine gabbros). By contrast, in the Maqsad MTZ samples the trace element compositions of olivine, clinopyroxene and plagioclase show the lowest REE concentrations in the most evolved *MTZ olivine gabbros* (Fig. 7). The discrepancies between modal compositions and mineral major and trace element features thus rule out a genetic relationship between the two groups and the initially envisioned process of fractional crystallization within sills for the MTZ gabbroic layers.

The most striking chemical features differentiating the two sample groups, in addition to the modal compositions, are major element compositional trends of mineral phases. Consistently with the results of textural evolution between *MTZ impregnated dunites* and *MTZ olivine gabbros* (Higgie and Tommasi 2012), we here assess that all layers have formed through a single process of reactive percolation, but that positive feedback between deformation and melt distribution allowed for variations in melt/rock ratios and

percolation intensity at the centimetre-scale (Fig. 8). In the following, we document the interplays between reaction (crystallization, dissolution), melt fluxes (melt localization, redistribution, and renewal) and the evolution of the structure of reacting domains (deformation, porosity), before providing chemical models of compositional evolution of the percolated matrix to constrain the control of the melt/rock ratios and melt fluxes on the evolution of the magmatic system. Our hypotheses are that: (i) the composition of the interstitial melt was dominated by the crystal matrix in the *MTZ impregnated dunites*, and that (ii) enhanced permeability and melt percolation within the actively deforming layers accounted for the formation of the *MTZ olivine gabbros*, in a magmatic system dominated by the incoming melt composition.

Diffuse melt percolation in MTZ impregnated dunite layers

The *MTZ impregnated dunites* best preserve the microstructure and chemical composition of the precursor dunites; they show fewer evidence of dissolution microstructures (Figs. 2a and b and 3a, b and c) and the olivine matrix preserves the axial-[100] olivine CPO, typical of high-temperature deformation under melt-free conditions (Ben Ismail and Mainprice 1998; Tommasi et al. 2000). Olivine from *MTZ impregnated dunites* shows Forsterite contents similar to MTZ dunites (Fo = 87–89 mol%; Rospabé et al. 2018; Kelemen et al. 2020; Kourim et al. 2022), even in samples composed of only ~ 50 vol% olivine (Figs. 4 and 5). Preservation of the precursor dunite composition implies that the olivine matrix was mildly reequilibrated with the percolating melts at the most. It is worth noting that olivine and clinopyroxene display Mg-Fe equilibrium within the *MTZ impregnated dunite* layers (Supplementary Figure S5). This in turn suggests that rather than being reequilibrated with the percolating melt, the olivine matrix buffered the percolating melt towards elevated Mg-numbers. We argue that this lack of reequilibration of the olivine matrix in the *MTZ impregnated dunite* layers results from low melt/rock ratios integrated over time within these layers, and to a magmatic system characterized by scarce melt renewal, in which compositions were dominated by the dissolution-precipitation reaction (see Ionov et al. 2005 and *Discussion* section 7.2 for modeling of the reequilibration process). This is further supported by slightly more evolved compositions of interstitial clinopyroxene and plagioclase, with decreasing Anorthite contents and slightly increasing HREE contents in clinopyroxene and olivine (Figs. 6 and 7). Such compositional variations result from higher degrees of fractionation of the percolating melt during reactive melt percolation (e.g., Dick et al. 2002; Miller et al. 2009) with respect to the *MTZ olivine gabbro* layers. Notably, the chemical trend defined by

constant olivine Forsterite at decreasing plagioclase Anorthite contents (Fig. 6) is mirrored by MELTS models of reactive crystallization involving extensive olivine dissolution; while olivine Forsterite content is buffered by extensive dissolution of the dunitic matrix, plagioclase composition can evolve freely during melt fractionation (see AFC models in Fig. 6; e.g., Basch et al. 2019). Nevertheless, although melt fractionation is slightly stronger than in *MTZ olivine gabbro* layers, the trace element compositions remain primitive in *MTZ impregnated dunites* and no strong increase in clinopyroxene Zr_N/Nd_N is observed.

Progressive reaction-driven evolution of the melt composition during fractional crystallization is in line with a process of diffuse melt impregnation, during which single melt aliquots fractionate as they pond and react with the crystal matrix. Such a process of melt impregnation is also consistent with the high clinopyroxene Cr_2O_3 contents documented in the *MTZ impregnated dunites* (Fig. 5c). This feature is commonly reported as evidence for melt-rock interaction processes involving partial assimilation of primitive Cr-spinel-bearing assemblages in deep-seated magmatic systems (Mid-Atlantic Ridge: Lissenberg and Dick 2008; Boulanger et al. 2024; Southwest Indian Ridge: Zhang et al. 2020; Ferrando et al. 2021a; Erro-Tobbio ophiolite: Borghini and Rampone 2007; Rampone et al. 2016; experimental constraints: Van den Bleeken, 2010; Yang et al. 2019). The partial preservation of primitive olivine compositions in all *MTZ impregnated dunites* ($Fo=87.3-89.0$ mol%; Fig. 4) thus advocates for limited reequilibration between the crystal matrix and the percolating melt, in a system which composition was dominated by the crystal matrix and dissolution-precipitation processes.

Such matrix-dominated magmatic systems involving modification of the melt composition during reaction processes have been widely documented in the lower oceanic crust. One of the best documented example of such reactive processes is the formation of replacive olivine-rich troctolites through reaction between a dunitic matrix and percolating melts. This hybridization process has been reported in the modern oceanic lithosphere (e.g., Mid-Atlantic Ridge: Suhr et al. 2008; Drouin et al. 2009, 2010; Ferrando et al. 2018, 2020; Boulanger et al. 2024; Parece Vela back-arc spreading ridge: Sanfilippo et al. 2013), ophiolitic settings (Alpine-Apennine ophiolites: Renna and Tribuzio 2011; Sanfilippo et al. 2014; Rampone et al. 2016; Basch et al. 2018, 2019, 2021; East Taiwan ophiolite: Morishita et al. 2018), and has been reproduced experimentally (Van den Bleeken et al. 2010; Tursack and Liang 2012; Saper and Liang 2014; Borghini et al. 2018; Yang et al. 2019). Notably, although the modal composition and formation process of all these olivine-rich troctolites are similar, with progressive dissolution of an olivine matrix during crystallization

of interstitial plagioclase and clinopyroxene, olivine-rich troctolites worldwide show drastically different microstructural and chemical features, from preservation to complete reequilibration of the precursor CPO and chemical composition. We argue that the preservation or evolution of the latter features are directly correlated to the physical parameters involved in the melt reactive percolation process, i.e., the percolation intensity and the instantaneous and time-integrated melt/rock ratios. At the Atlantis Massif OCC, along the Mid-Atlantic Ridge, olivine-rich troctolites show strong modifications of the olivine matrix CPO (Drouin et al. 2010; Ferrando et al. 2018) and effective chemical reequilibration during impregnation of precursor dunites involving high instantaneous and time-integrated melt/rock ratios (Drouin et al. 2009; Ferrando et al. 2020; Boulanger et al. 2024). These microstructural and chemical modifications during hybridization of the Atlantis Massif dunites are indicative of a melt-dominated magmatic system, in which the matrix was reequilibrated with the percolating melt without strong compositional modification of the latter. On the contrary, olivine-rich troctolites from the Erro-Tobbio ophiolite, in the Ligurian Alps, show preserved and constant composition of the olivine matrix within hybridized troctolitic samples, regardless of olivine modal contents (Rampone et al. 2016; Basch et al. 2019). Similar to what we document in the *MTZ impregnated dunites* (Figs. 4, 5a and b and 7a), the preservation of the olivine matrix compositions in the Erro-Tobbio olivine-rich troctolites is correlated with strong compositional variability of interstitial minerals, such as decreasing plagioclase Anorthite contents and increasing clinopyroxene Cr_2O_3 concentrations. These compositional features, together with the preservation of the olivine matrix axial-[100] CPO, suggest that the hybridization occurred in a magmatic system dominated by the crystal matrix for both the Erro-Tobbio ophiolite and our samples of *MTZ Impregnated dunites*.

Focused percolation in MTZ olivine gabbro layers

MTZ olivine gabbros show the strongest olivine grain size reduction and dissolution features (Figs. 2c and d and 3d, e and f), and correspond to the most hybridized samples during the melt percolation process forming the Maqсад MTZ layering (Fig. 8; Higgle and Tommasi 2012). *MTZ olivine gabbros* show relatively homogeneous and primitive mineral chemical compositions, broadly fitting with the most primitive end of fractional crystallization trends of hydrous N-MORB melts (Fig. 6; MELTS models following MacLeod et al. 2013; see caption for modeling detail). Even within the most olivine-poor sample (12 vol% olivine), major element compositions of mineral phases fit within the initial 20% fractionated mass of a primitive melt (Fig. 6).

Low trace element contents within the interstitial phases are also consistent with these small amounts of fractionation of the parental melt (Figs. 7 and 9b). Such homogeneous and primitive compositions of the interstitial phases crystallized in *MTZ olivine gabbro* layers are the expression of the open-system character of the reactive melt migration process, during which each single MORB-type melt aliquot dissolved only a small fraction of the percolated matrix and fractionated a small amount of its mass before being extracted from the sample and replaced by a new melt increment. Notably, positive Sr/Sr* anomalies in interstitial clinopyroxenes (Fig. 7b) suggest that the reactive percolation process driving the hybridization of the dunitic matrix likely involved partial dissolution of olivine together with minor amounts of plagioclase, in turn leading to Sr enrichments within the reactive melt and crystallized phases. Conversely, clinopyroxene Zr_N/Nd_N ratios, widely recognized as an efficient tracer of melt/rock interaction processes (e.g. Ferrando et al. 2021a; Basch et al. 2024), remain low and comparable to the most primitive gabbroic samples from Oman, Hess Deep and Atlantis Bank (Fig. 9b). This further substantiates that the reaction process, although locally driving Sr enrichments, did not buffer the melt composition and that the amount of olivine dissolution was not able to drive Zr-Hf over-enrichments in the melt phase (see Rampone et al. 2016, 2020; Sanfilippo et al. 2020; Basch et al. 2022; Ferrando et al. 2021a).

In this progressive hybridization scenario, olivine in the *MTZ olivine gabbros* did not all crystallize from the percolating melt but at least in part represents the pre-existing solid matrix that was partially dissolved and reequilibrated during the reactive percolation process. It is worth noting that olivine most likely recrystallized from the percolating melt during the dissolution-recrystallization process. Yet, olivine is characterized by relatively homogeneous major and trace element compositions, clearly distinct from those within the *MTZ impregnated dunites* (Fig. 4); it shows relatively low Forsterite, Ni and REE, high Mn contents (Figs. 5a and b and 7a), and no core-to-rim zonation in olivines showing clear dissolution features (Supplementary Figure S4). Olivine is in Mg-Fe equilibrium with clinopyroxene crystallized from the interstitial melt (Supplementary Figure S5), in turn indicating that the relict olivine matrix was efficiently reequilibrated with the percolating melt during continuous melt migration. In this context of efficient melt renewal, such complete reequilibration of the olivine matrix most likely resulted from processes of melt/rock interaction integrated over time (see *Discussion section 7.2* for modeling of the reequilibration process). Furthermore, the preservation of a clear olivine axial-[010] CPO pattern indicates that the instantaneous melt/rock ratios remained low and did not reach the critical value allowing for the loss of cohesion of

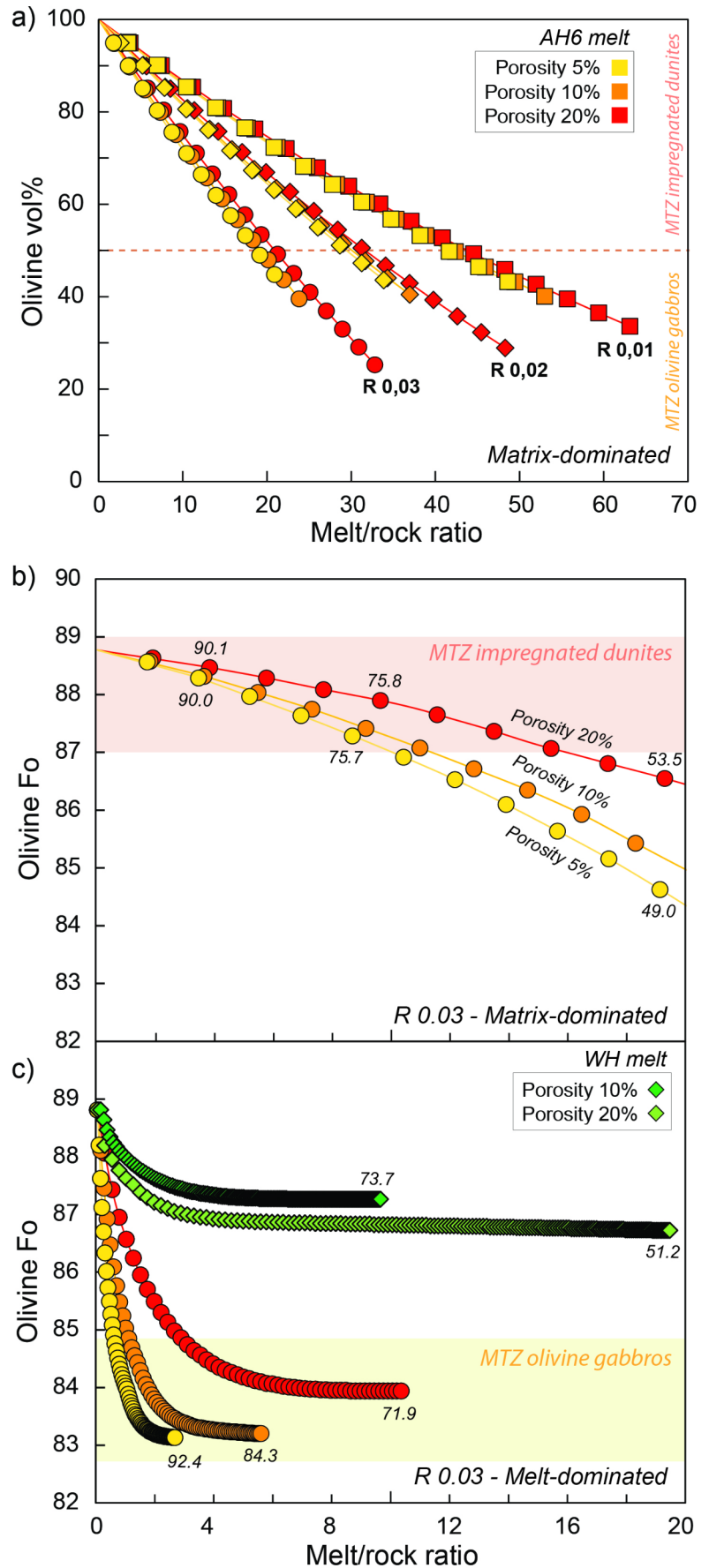
the solid matrix (20–40% instantaneous melt fraction; e.g., Rosenberg and Handy 2005; Higginson and Tommasi 2012). Shear-induced melt focusing thus promoted iterative and continuous chemical exchange between the percolated matrix and a limited proportion of migrating melt. In these layers, the major and trace element compositions of both the interstitial phase and the reequilibrated olivine matrix were driven by the composition of the incoming melt rather than buffered by the dissolution-precipitation reaction.

Mg# modeling of reactive melt percolation

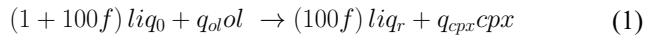
To assess the compositional evolution of a dunitic matrix and quantify melt/rock ratios involved during (i) diffuse melt impregnation, and (ii) focused reactive melt percolation, we performed numerical simulations of olivine-dissolving melt-rock interaction processes using the *Plate Model* of Vernières et al. (1997) modified for modelling Mg-numbers (see Bedini et al. 2002; Ionov et al. 2005; Bodinier et al. 2008). The *Plate Model* has been designed to compute the progressive chemical reequilibration of a melt phase and a percolated rock column during reactive percolation processes. The model simulates iterative steps of dissolution and concomitant crystallization, in turn modifying the porosity of the system and the melt/rock ratio involved in the reaction process. Furthermore, the *Plate Model* allows us to evaluate the impact of melt renewal on chemical reequilibration; at low melt flux, the incoming melt is buffered by the solid matrix, while at high flux conditions, the melt phase dominates the composition of the magmatic system. Hence, to assess the control of these physical parameters on the chemical evolution of the melt and percolated rock, we here performed reactive percolation models involving variable porosities (i.e., melt/rock ratio) and melt fluxes.

As discussed by Hanson and Langmuir (1978), Mg and Fe can be considered as trace elements during melt-rock interaction processes; an approach based on partition coefficients can thus be applied to the modeling, provided that the stoichiometry of the solid phases is respected (e.g. the sum $MgO + FeO$ in olivine must be kept constant at 66.67 mol%). In turn, the mineral stoichiometry imposes strong limitations on the extent of Mg-Fe exchange between solid and liquid phases. To avoid the stoichiometry violation, the total inverse method from Tarantola and Valette (1982) is used to constrain Mg-Fe redistribution between solid and liquid phases after each reaction increment, following the method described in Bedini et al. (2002) and Ionov et al. (2005). Mg and Fe mineral/melt partition coefficients were fixed after Ulmer (1989) for a pressure of 2 kbar and a temperature of 1200 °C, and are allowed to vary during numerical simulations to account for Mg and Fe variations in the melt phase, based on experimental constraints (Ulmer 1989).

Fig. 10 Results of numerical simulations of reactive melt percolation using the *Plate Model* (Vernières et al. 1997) adapted for Mg# by Bedini et al. (2002). Residual mass fraction f is fixed to 0.99, the mass ratio of crystallized clinopyroxene to incoming melt R varies between 0.01 and 0.03, porosity ϕ varies between 5% and 20%, and the initial melt composition is AH6 N-MORB melt (Mg# = 61.8) after Husen et al. (2016). **a** Melt/rock ratio vs. olivine modal content of iterative low-flux model assuming different reactivity of the magmatic system ($R=0.01-0.03$). Each symbol along a single trend corresponds to a melt recharge and new incremental run of the reactive process (see text for detail); **b** Melt/rock ratio vs. olivine Fo of iterative low-flux models at $R=0.03$ and variable porosity (5-10-20%). Each symbol along a single trend corresponds to a melt recharge, porosity reopening (Supplementary Fig. S5) and new incremental run of the reactive process. Numbers along the curves indicate the olivine modal content of the specific model iteration; **c** Melt/rock ratio vs. olivine Fo of high-flux reactive melt percolation at $R=0.03$ and variable porosity (5-10-20%). Numbers at the tip of curves indicate the olivine modal content at the end of the reactive model. Also shown are the high-flux percolation models using the same parameters but a more primitive initial melt composition after Workman and Hart (2005), Mg# = 68.3. The coloured boxes represent the composition of the analysed *MTZ impregnated dunites* and *MTZ olivine gabbros*



Following petrographic and textural constraints, we modeled diffuse and focused open-system reactive percolation involving the crystallization of clinopyroxene at the expense of the interstitial melt and the pre-existing olivine matrix, following the reaction:



in which liq_0 and liq_r represent the incoming and reacted melt, respectively, f is the residual mass fraction of melt after each reaction increment (with f ranging from 0 to 1), and q_{ol} and q_{cpx} the dissolved and crystallized mass of olivine and clinopyroxene, respectively (with $q_{ol} + q_{cpx} = 1$) (Vernières et al. 1997). All models were performed at decreasing melt mass, with f arbitrarily fixed at 0.99, meaning that each reaction increment decreased the initial melt fraction by 1%. We simulated the reactive melt percolation process at different porosities ($\phi = 5\text{--}20\%$) and different mass ratios of crystallised minerals to incoming melt ($R = 0.01\text{--}0.03$). Notably, variations of the latter parameter $R = q_{cpx} / (1 + 100f)$ at fixed f implies that the increased crystallised mass of clinopyroxene is balanced by dissolution of olivine; the higher the R parameter is, the more intense the reactive process will be. Furthermore, to assess the impact of initial melt composition on the evolution of the magmatic system, we computed reactive melt percolation within a dunitic matrix ($\text{Fo} = 88.8 \text{ mol}\%$) using two different initial melt compositions characterized by variable Mg-numbers, (i) AH6 tholeiitic after Husen et al. (2016), $\text{Mg}\# = 61.8$; (ii) primitive N-MORB after Workman and Hart (2005), $\text{Mg}\# = 68.3$.

To simulate focused melt percolation within a deforming rock, similar to what Higgie and Tommasi (2012) described for the *MTZ olivine gabbro* layers, the matrix-dominated percolation models were performed with successive iterations at low melt flux, using for each increment the output of the previous reaction step as initial matrix composition. Additionally, at each iteration the porosity and incoming melt composition were reset to their initial values (i.e., AH6 incoming melt composition, 5, 10, 20% porosity, see Supplementary Figure S6), simulating constant re-opening of the system.

Low-flux diffuse melt impregnation

The Fig. 10a illustrates the impact of variable extents of the dissolution-precipitation process (i.e., of increasing iterations and time-integrated melt/rock ratio) on the progressive evolution in modal composition of the percolated matrix. More intense reaction ($R = 0.03$) leads to more efficient dissolution of the olivine matrix and thus requires lower melt/rock ratios integrated over time to account for the range of olivine modal compositions characterizing the

MTZ impregnated dunites. More intense reaction is also more efficient in driving the chemical reequilibration of the percolated matrix. Another key parameter in controlling the reequilibration of the olivine matrix is the porosity of the system. Considering constant reaction parameters (fixed f , R , q_{ol} and q_{cpx}), a given $\text{Mg}\#$ of the reequilibrated matrix is obtained at lower melt/rock ratios for low porosities (Fig. 10b). Yet, it is worth noting that to reequilibrate the matrix, low porosities require higher melt pore volume, which represents the ratio between melt/rock ratio and porosity, i.e., the number of times the porosity is filled with new incoming melt (Supplementary Figure S7). Figure 10b shows that for a highly porous dunitic matrix (20% porosity), even at a melt/rock ratio integrated over time of ~ 20 (pore volume = 100; Supplementary Figure S7) and after dissolution of more than 40 vol% olivine, the remaining olivine matrix is far from equilibrium with the input melt ($\text{Mg}\# = 61.8$, equilibrium olivine $\text{Fo} = 83 \text{ mol}\%$; Fig. 10b). These models thus substantiate that low-flux melt percolation processes are not efficient in reequilibrating the reacted matrix with the incoming melt, but rather the contrary.

High-flux focused melt percolation

The Fig. 10c shows the results of the high-flux melt percolation models, using similar parameters to the previous low-flux models. In this melt-dominated system, complete reequilibration of the olivine matrix is attained. Namely, a highly porous dunite (20% porosity) fully reequilibrates with the incoming melt at a time-integrated melt/rock ratio of ~ 10 , after 28 vol% of the olivine matrix is dissolved. A less porous dunitic matrix (5% porosity) is reequilibrated at melt/rock ratios as low as ~ 2.5 (yellow trend in Fig. 10c), after dissolving only 8 vol% of the olivine matrix. Notably, the extensive olivine dissolution associated with the high-porosity models seemingly lead to a buffer of the melt compositions by the reactive process, in turn leading to slightly higher equilibrium Fo contents ($\text{Fo}_{\text{equ}} = 83.9 \text{ mol}\%$ for 20% porosity, $\text{Fo}_{\text{equ}} = 83.1 \text{ mol}\%$ for 5% porosity). These models therefore clearly indicate that focused and high-flux reactive melt percolation is drastically more efficient than low-flux processes in reequilibrating the percolated matrix. Notably, the preservation of the precursor olivine composition at decreasing modal olivine in *MTZ Impregnated dunites* is not compatible with reequilibration during high-flux melt percolation (Fig. 10c), but rather require low-flux melt migration.

The same reactive percolation models were performed using a primitive N-MORB melt (green trends in Fig. 10c; melt composition after Workman and Hart 2005) and did not allow to fit the olivine composition analysed in *MTZ olivine gabbros* ($\text{Fo} = 83\text{--}84 \text{ mol}\%$; Supplementary Table S1).

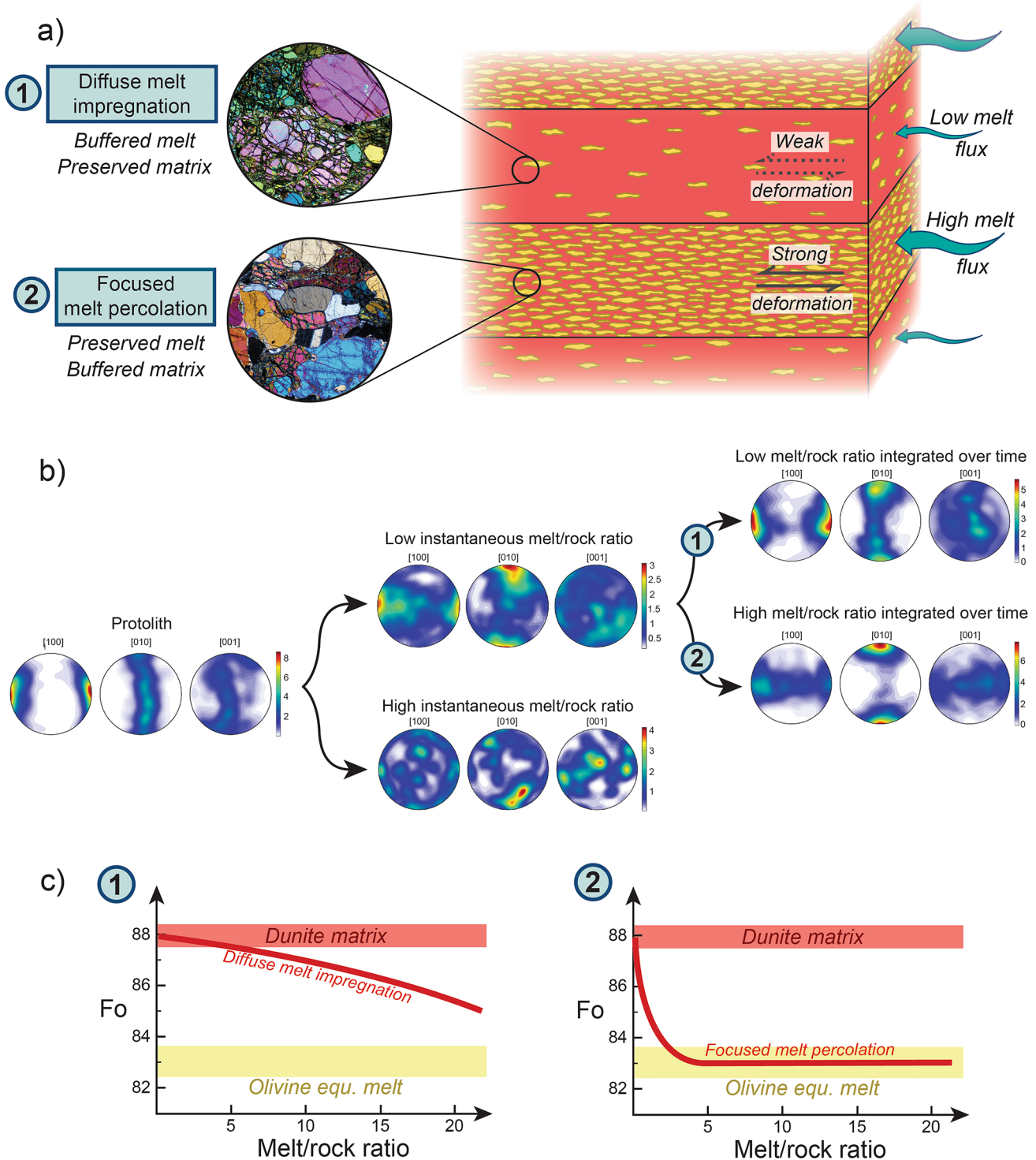


Fig. 11 Control of percolation dynamics and melt/rock ratios on the structural and chemical evolution of a magmatic system; **a** Synthetic sketch of the formation of the Maqsad Massif MTZ layering, after focused melt percolation within actively deforming layers, in turn driving the development of high- and low-flux magmatic processes; **b** Evolution of olivine CPO during reactive melt migration processes. Dunite protolith from the Oman MTZ is presented as a starting point (Higgie and Tommasi 2012). CPO developed after low and high

instantaneous melt/rock ratios are from Erro-Tobbio olivine-rich troctolites (Basch et al. 2019). CPO indicative of low and high melt/rock ratios integrated over time are respectively from *MTZ impregnated dunites* and *MTZ olivine gabbros* from Oman Maqsad Massif (Higgie and Tommasi 2012); **c** Summary of the Plate Models, showing the evolution of Forsterite content at increasing melt/rock ratio integrated over time for processes of diffuse melt impregnation and focused melt percolation

Instead, in these models, the matrix reequilibrated with the incoming melt composition only shows slightly decreasing Forsterite contents upon percolation of the melt with Mg# = 68.3 (after Workman and Hart 2005). A slightly more evolved melt, akin AH6 with Mg# = 61.8 (after Husen et al. 2016) and similar to parental melts to the Oman lowermost gabbros (see Garbe-Schönberg et al. 2022d Iler et al., 2022), is therefore required to allow for the reequilibration of the *MTZ olivine gabbros*.

It is worth noting that in the Maqсад MTZ, the positive feedback between deformation and melt distribution leads to constant and focused melt percolation within the *MTZ olivine gabbro* layers (Fig. 8), implying that the melt flux and associated melt/rock ratios integrated over time within these layers are likely to be elevated, and easily sufficient for fully reequilibrating the percolated matrix (melt/rock ratios ranging between ~ 2.5 and 10; Fig. 10c). Conversely, the diffuse melt percolation process forming the *MTZ impregnated dunite* layers does not bear continuous melt percolation and is unlikely to reach the elevated melt/rock ratios required for complete reequilibration of the percolated matrix (i.e., melt/rock ratios > 20; Fig. 10b).

Control of melt/rock ratios and melt flux on structural and chemical evolution

Deformation-assisted melt distribution within the Oman MTZ led to drastic variability in porosity and melt flux at the centimetre-scale, during reactive melt percolation processes, from focused percolation within highly porous layers and diffuse impregnation of undeformed dunite portions (Fig. 8). This in turn allows to constrain the control of melt fluxes on the structural and geochemical evolution of a common dunitic precursor.

Focused deformation drove continuous and intense melt percolation within the *MTZ olivine gabbro* layers (Supplementary Figure S5), while allowing for the preservation of the dunitic protolith within the *MTZ impregnated dunite* layers (Fig. 11a). Consistently, these processes led to the respective modification and preservation of the pre-existing olivine matrix CPO (Fig. 2). Figure 11b provides an overview of the control of melt/rock ratios, both instantaneous and integrated over time, on the structure of a percolated matrix. Starting from the initial dunitic matrix characterized by axial-[100] olivine CPO, as developed after high-temperature low-strain deformation, percolation of melt at elevated instantaneous melt/rock ratios leads to the disaggregation of the solid matrix, in turn driving a loss of the pre-existing structure. Conversely, when melt/rock ratios are kept below the disaggregation threshold (~ 20–40 vol%; Rosenberg and

Handy, 2005), the preservation or modification of the matrix CPO is a function of the melt/rock ratios integrated over time. In the Maqсад MTZ, elevated melt/rock ratios associated to focused percolation within *MTZ olivine gabbro* layers drive the development of an axial-[010] olivine CPO (Fig. 2c, d; Higgie and Tommasi 2012), while low-flux diffuse melt input within the *MTZ impregnated dunite* layers allows for the preservation of the initial axial-[100] CPO (Fig. 11b).

In association with such microstructural evolution, elevated melt/rock ratios integrated over time drive the complete reequilibration of the chemical system only in the case of a focused, high-flux melt percolation (Figs. 10c and 11c). Our *Plate Models* demonstrate that low-flux diffuse magmatic systems, in which the melt composition is strongly buffered by the solid matrix, require very elevated melt/rock ratios (> 20) to allow for the full reequilibration of the composition of the percolated matrix (Fig. 10b). Notably, while at low instantaneous melt/rock ratios, the preservation or modification of the matrix CPO directly indicates the extent of integrated melt/rock ratios, only mineral chemistry can give insights on the dynamics of the percolation process once the disaggregation threshold has been reached at high instantaneous melt/rock ratios.

Summary and conclusions

Deformation-driven focused percolation within the Oman Moho Transition Zone offers a unique opportunity to assess the control of percolation intensity and melt/rock ratios on the structural and chemical evolution of a percolated matrix. In low-flux magmatic systems akin to the *MTZ impregnated dunitites*, the structure and geochemical composition of the protolith are preserved, and the melt composition is buffered by the solid matrix and dissolution-precipitation reaction. Conversely, continuous and high-flux reactive melt percolation as documented within the *MTZ olivine gabbros* leads to the modification of the matrix CPO and to the complete chemical reequilibration of the olivine matrix; the matrix is easily buffered by the composition of the incoming melt and reactive processes exert limited control on the liquid line of descent. This in turn implies that only melts involved in low-flux magmatic systems can drive significant modification of the tholeiitic melts during their upwards reactive percolation. Furthermore, we here provide a global overview of the evolution of the composition and texture of an olivine-rich protolith as a function of the percolation dynamics and the involved melt/rock ratios, both instantaneous and integrated over time.

Supplementary Information The online version contains supplementary material available at <https://doi.org/10.1007/s00410-024-02194-1>.

Acknowledgements The authors thank Andrea Risplendente for assistance with EPMA analyses and Olivier Bruguier (AETE-ISO facility, OSU OREME, University of Montpellier) for assistance with LA-ICP-MS analyses. The authors also thank two anonymous reviewers for constructive reviews that increased the clarity of the manuscript, and Dante Canil for editorial handling.

Funding This research was funded by the Italian Ministry of University and Research (MUR) through ECORD-IODP Italia with the ECORD-IODP Italia 2021 grant awarded to Valentin Basch, by the People Programme (Marie Curie Actions) of the European Union's Seventh Framework Programme FP7/2007–2013/under REA-Grant Agreement No. 608001 'ABYSS', and by the "Progetti di Rilevante Interesse Nazionale" PRIN2022PC9NME_TRANSIENT funded by the MUR and European Union—Next Generation EU.

Data availability The mineral chemistry reported in this article will be made available as Supplementary Material as well as on the GFZ database at the following reference: *Basch, V., Godard, M., Tommasi, A., Rampone, E. (2024) Database of mineral compositions within the Oman Moho Transition Zone layered gabbros (Maqсад Massif, Oman ophiolite). GFZ Data services, doi: to be attributed.*

Declarations

Conflict of interest The authors declare that they have no known financial competing interests nor personal conflict of interest.

References

- Abily B, Ceuleneer G (2013) The dunitic mantle-crust transition zone in the Oman ophiolite: residue of melt-rock interaction, cumulates from high-MgO melts, or both? *Geology* 41:67–70. <https://doi.org/10.1130/G33351.1>
- Basch V, Rampone E, Crispini L, Ferrando C, Ildefonse B, Godard M (2018) From mantle peridotites to hybrid troctolites: textural and chemical evolution during melt-rock interaction history (Mt. Maggiore peridotites, Corsica, France). *Lithos* 323:4–23. <https://doi.org/10.1016/j.lithos.2018.02.025>
- Basch V, Rampone E, Crispini L, Ferrando C, Ildefonse B, Godard M (2019) Multi-stage reactive formation of troctolites in a fossil slow-spreading oceanic lithosphere: a combined field and petrochemical study (Erro-Tobbio ophiolite, Italy). *J Petrol* 60:873–906. <https://doi.org/10.1093/petrology/egz019>
- Basch V, Drury MR, Plumper O, Hellebrand E, Crispini L, Barou F, Godard M, Rampone E (2021) Intracrystalline melt migration in deformed olivine revealed by trace element compositions and polyphase solid inclusions. *Eur J Mineral* 33:463–477. <https://doi.org/10.5194/ejm-33-463-2021>
- Basch V, Sanfilippo A, Skolotnev S, Ferrando C, Muccini F, Palmiotto C, Peyve AA, Ermolaev BV, Okina OI, Ligi M (2022) Genesis of oceanic oxide gabbros and gabbro-norites during reactive melt migration at transform walls (Doldrum Megatransform System; 7–8°N Mid-atlantic Ridge). *J Petrol* 63:1–23. <https://doi.org/10.1093/petrology/egac086>
- Basch V, Ferrando C, Sanfilippo A (2023) A frozen oceanic crystal mush. *Terra Nova*. <https://doi.org/10.1111/ter.12655>
- Basch V, Sanfilippo A, Snow JE, Loocke M, Zanetti A (2024) Accretion of the lower oceanic crust at fast-spreading ridges: insights from Hess Deep (East Pacific rise, IODP Expedition 345). *J Petrol* 65. <https://doi.org/10.1093/petrology/egae048>
- Bedini RM, Bodinier J-L, Vernières J (2002) Numerical simulation of Mg-Fe partitioning during melting and melt-rock reaction in the shallow upper mantle. Extended Abstracts, Proceedings of 4th International Orogenic Lherzolites and Mantle Processes Conference. Japan: Samani (unpublished)
- Belgrano TM, Diamond LW (2019) Subduction-zone contributions to axial volcanism in the Oman-U.A.E. ophiolite. *Lithosphere* 11:399–411. <https://doi.org/10.1130/L1045.1>
- Belgrano TM, Diamond LW, Vogt Y, Biedermann AR, Gilgen SA, Al-Tobi K (2019) A revised map of volcanic units in the Oman ophiolite: insights into the architecture of an oceanic proto-arc volcanic sequence. *Solid Earth* 10:1181–1217. <https://doi.org/10.5194/se-10-1181-2019>
- Ben Ismail W, Mainprice D (1998) An olivine fabric database: an overview of upper mantle fabrics and seismic anisotropy. *Tectonophysics* 296:145–157. [https://doi.org/10.1016/S0040-1951\(98\)0141-3](https://doi.org/10.1016/S0040-1951(98)0141-3)
- Beurrier M, Ohnenstetter M, Cabanis B, Lescuyer JL, Tegye M, Le Metour J (1989) Géochimie des filons doléritiques et des roches volcaniques ophiolitiques de la nappe de Semail; contraintes sur leur origine géotectonique Au Crétacé supérieur. *Bull De La Société Géologique De France* 2:205–219. <https://doi.org/10.2113/gssgfbull.V.2.205>
- Bodinier J-L, Garrido CJ, Chanefo I, Bruguier O, Gervilla F (2008) Origin of pyroxenite-peridotite veined mantle by refertilization reactions: evidence from the Ronda Peridotite (Southern Spain). *J Petrol* 49:999–1025. <https://doi.org/10.1093/petrology/egn014>
- Borghini G, Rampone E (2007) Postcumulus processes in oceanic-type olivine-rich cumulates: the role of trapped melt crystallization versus melt-rock interaction. *Contrib Miner Petrol* 154:619–633. <https://doi.org/10.1007/s00410-007-0217-5>
- Borghini G, Francomme JE, Fumagalli P (2018) Melt-dunite interactions at 0.5 and 0.7GPa: experimental constraints on the origin of olivine-rich troctolites. *Lithos* 323. <https://doi.org/10.1016/j.lithos.2018.09.022>
- Boudier F, Nicolas A (1985) Harzburgite and lherzolite subtypes in ophiolitic and oceanic environments. *Earth Planet Sci Lett* 76:84–92
- Boudier F, Nicolas A (1995) Nature of the Transition Zone in the Oman Ophiolite. *J Petrol* 36:777–796
- Boudier F, Ceuleneer G, Nicolas A (1988) Shear zones, thrusts and related magmatism in the Oman ophiolite: initiation of thrusting on an oceanic ridge. *Tectonophysics* 151:275–296. [https://doi.org/10.1016/0040-1951\(88\)90249-1](https://doi.org/10.1016/0040-1951(88)90249-1)
- Boudier F, Nicolas A, Ildefonse B (1996) Magma chambers in the Oman ophiolite: fed from the top and the bottom. *Earth Planet Sci Lett* 144:239–250
- Boudier F, Nicolas A, Ildefonse B, Jousset D (1997) EPR microplates, a model for the Oman ophiolite. *Terra Nova* 9:79–82
- Boulanger M, France L (2023) Cumulate formation and melt extraction from mush-dominated Magma reservoirs: the Melt flush process exemplified at Mid-ocean Ridges. *J Petrol* 64:egad005. <https://doi.org/10.1093/petrology/egad005>
- Boulanger M, France L, Deans JRL, Ferrando C, von der Lissenberg CJ (2020) Magma Reservoir formation and evolution

- at a slow-spreading Center (Atlantis Bank, Southwest Indian Ridge). *Front Earth Sci* 8:554598. <https://doi.org/10.3389/feart.2020.554598>
- Boulanger M, France L, Ferrando C, Ildefonse B, Ghosh B, Sanfilippo A, Liu C-Z, Morishita T, Koepke J, Bruguier O (2021) Magma-mush interactions in the lower oceanic crust: insights from Atlantis Bank layered series (Southwest Indian Ridge). *J Geophys Res: Solid Earth.*, 126, e2021JB022331 <https://doi.org/10.1029/2021JB022331>
- Boulanger M, Godard M, Ildefonse B, Bakouche M (2024) Petrological evidence for prominent melt-mush reactions during slow-spreading oceanic accretion. *Geochem Geophys Geosyst.* 25, e2023GC011409 <https://doi.org/10.1029/2023GC011409>
- Browning P (1982) PhD thesis: The petrology, geochemistry, and structure of the plutonic rocks of the Oman Ophiolite. The Open University, Milton Keynes
- Browning P (1984) Cryptic variations within the cumulate sequence of the Oman ophiolite: Magma chamber depth and petrological implications. *Geol Soc Lond Special Publication* 13:71–82
- Cashman KV, Sparks RSJ, Blundy JD (2017) Vertically extensive and unstable magmatic systems: a unified view of igneous processes. *Science* 355:eaag3055. <https://doi.org/10.1126/science.aag3055>
- Cheadle MJ, Gee JS (2017) Quantitative textural insights into the formation of gabbro in mafic intrusions. *Elements* 13:409–414. <https://doi.org/10.2138/gselements.13.6.409>
- Coogan LA, Dosso SE (2016) Quantifying parental MORB trace element compositions from the eruptive products of realistic magma chambers: parental EPR MORB are depleted. *J Petrol* 57:2105–2126. <https://doi.org/10.1093/petrology/egw059>
- Demouchy S, Alard O (2021) Hydrogen, trace, and ultra-trace element distribution in natural olivines. *Contrib Miner Petrol* 176. <https://doi.org/10.1007/s00410-021-01778-5>
- Dick HJB, Ozawa K, Meyer PS, Niu Y, Robinson PT, Constantin M et al (2002) Primary silicate mineral chemistry of a 1.5-km section of very slow spreading lower ocean crust: ODP Hole 735B, Southwest Indian Ridge. In: Natland JH, Dick HJB, Miller DJ, Von Herzen RP (eds) *Proc. ODP, Sci. Results vol. 176, Chap. 10. Ocean Drilling Program, College Station, Texas*, pp 1–61
- Dick HJB, Natland JH, Ildefonse B (2006) Past and future impact of Deep Drilling in the Ocean Crust and Mantle: an evolving Order out of New Complexity. *Oceanography* 19:72–80
- Dijkstra AH, Drury MR, Frijhoff RM (2002) Microstructures and lattice fabrics in the Hilti mantle section (Oman Ophiolite): evidence for shear localization and melt weakening in the crust–mantle transition zone? *J Phys Res* 107(B11):2270. <https://doi.org/10.1029/2001JB000458>
- Drouin M, Godard M, Ildefonse B, Bruguier O, Garrido CJ (2009) Geochemical and petrographic evidence for magmatic impregnation in the oceanic lithosphere at Atlantis Massif, Mid-atlantic Ridge (IODP Hole U1309D, 30°N). *Chem Geol* 264:71–88. <https://doi.org/10.1016/j.chemgeo.2009.02.013>
- Drouin M, Ildefonse B, Godard M (2010) A microstructural imprint of melt impregnation in slow spreading lithosphere: olivine-rich troctolites from the Atlantis Massif, Mid-Atlantic Ridge, 30°N, IODP Hole U1309D, Geochemistry, Geophysics, Geosystems 11. Q06003. <https://doi.org/10.1029/2009GC002995>
- Edmonds M, Cashman KV, Holness M, Jackson M (2019) Architecture and dynamics of magma reservoirs. *Philosophical Trans Royal Soc* 377:20180298. <https://doi.org/10.1098/rsta.2018.0298>
- Einaudi F, Godard M, Pezard P, Cochemé J-J., Coulon C, Brewer T, Harvey P (2003) *Geochem Geophys Geosyst* 4(8608). <https://doi.org/10.1029/2002GC000362>
- Elthon D (1979) High magnesia liquids as the parental magma for ocean floor basalts. *Nature* 278:514–518
- Ernewein M, Pflumio C, Whitechurch H (1988) The death of an accretion zone as evidenced by the magmatic history of the Sumail ophiolite (Oman). *Tectonophysics* 151:247–274. [https://doi.org/10.1016/0040-1951\(88\)90248-X](https://doi.org/10.1016/0040-1951(88)90248-X)
- Ferrando C, Godard M, Ildefonse B, Rampone E (2018) Melt transport and mantle assimilation at Atlantis Massif (IODP Site U1309): constraints from geochemical modeling. *Lithos* 323:24–43. <https://doi.org/10.1016/j.lithos.2018.01.012>
- Ferrando C, Lynn KJ, Basch V, Ildefonse B, Godard M (2020) Retrieving timescales of oceanic crustal evolution at Oceanic Core Complexes: insights from diffusion modelling of geochemical profiles in olivine. *Lithos* 376–377. <https://doi.org/10.1016/j.lithos.2020.105727>
- Ferrando C, France L, Basch V, Sanfilippo A, Tribuzio R, Boulanger M (2021a) Grain size variations record segregation of residual melts in slow-spreading oceanic crust (Atlantis Bank, 57°E Southwest Indian Ridge). *J Geophys Res: Solid Earth* 126 e2020JB020997. <https://doi.org/10.1029/2020JB020997>
- Ferrando C, Basch V, Ildefonse B, Deans J, Sanfilippo A, Barou F, France L (2021b) Role of compaction in melt extraction and accumulation at a slow spreading center: microstructures of olivine gabbros from the Atlantis Bank (IODP Hole U1473A, SWIR). *Tectonophysics* 815:229001. <https://doi.org/10.1016/j.tecto.2021.229001>
- France L, Lombard M, Nicollet C, Berthod C, Debret B, Koepke J, Ildefonse B, Toussaint A (2021) Quantifying the Axial Melt Lens dynamics at the roof of oceanic magma reservoirs (dike/gabbro transition): Oman Drilling Project GT3 Site Survey. *J Geophys Res: Solid Earth* 126 e2020JB021496. <https://doi.org/10.1029/2020JB021496>
- Garbe-Schönberg D, Koepke J, Müller S, Mock D, Müller T (2022) A reference section through fast-spread Lower Oceanic Crust, Wadi Gideah, Samail Ophiolite (Sultanate of Oman): whole rock geochemistry. *J Geophys Res Solid Earth* 127 e2021JB022734. <https://doi.org/10.1029/2021JB022734>
- Ghiorso MS, Gualda GAR (2015) An H₂O–CO₂ mixed fluid saturation model compatible with rhyolite–MELTS. *Contrib Miner Petrol* 169. <https://doi.org/10.1007/s00410-015-1141-8>
- Godard M, Jousset D, Bodinier JL (2000) Relationships between geochemistry and structure beneath a palaeo-spreading centre: a study of the mantle section in the Oman ophiolite. *Earth Planet Sci Lett* 180:133–148
- Godard M, Dautria JM, Perrin M (2003) Geochemical variability of the Oman ophiolite lavas: relationship with spatial distribution and paleomagnetic directions. *Geochemistry, Geophysics, Geosystems.* <https://doi.org/10.1029/2002GC000452>
- Goodenough KM, Thomas RJ, Styles MT, Schofield DI, MacLeod CJ (2014) Records of Ocean Growth and Destruction in the Oman–UAE Ophiolite. *Elements* 10:109–114. <https://doi.org/10.2113/gselements.10.2.109>
- Grambling NL, Dygert N, Boring B, Jean MM, Kelemen PB (2022) Thermal history of lithosphere formed beneath fast spreading ridges: constraints from the mantle transition zone of the East Pacific Rise at Hess Deep and Oman Drilling Project, Wadi Zeeb, Samail ophiolite. *J Geophys Res: Solid Earth* 127 e2021JB022696. <https://doi.org/10.1029/2021JB022696>
- Guilmette C, Smit MA, van Hinsbergen DJJ, Gürer D, Corfu F, Charette B, Maffione M, Rabeau O, Savard D (2021) Forced subduction initiation recorded in the sole and crust of the Semail Ophiolite of Oman. *Nat Geosci* 11:688–695. <https://doi.org/10.1038/s41561-018-0209-2>
- Hanghøj K, Kelemen PB, Hassler D, Godard M (2010) Composition and genesis of depleted mantle peridotites from the Wadi Tayin Massif, Oman ophiolite; major and trace element geochemistry,

- and Os isotope and PGE systematics. *J Petrol* 51:201–227. <https://doi.org/10.1093/petrology/egp077>
- Hanson GN, Langmuir CH (1978) Modelling of major elements in mantle–melt systems using trace element approaches. *Geochim Cosmochim Acta* 42:725–742
- Higgle K, Tommasi A (2012) Feedbacks between deformation and melt distribution in the crust–mantle transition zone of the Oman ophiolite. *Earth Planet Sci Lett* 359–360:61–72. <https://doi.org/10.1016/j.epsl.2012.10.003>
- Holtzman BK, Kohlstedt DL, Zimmerman ME, Heidelbach F, Hiraga T, Hustoft J (2003) Melt segregation and strain partitioning: implications for seismic anisotropy and mantle flow. *Science* 301:1227–1230. <https://doi.org/10.1126/science.1087132>
- Husen A, Renat RA, Holtz F (2016) The effect of H₂O and pressure on multiple saturation and liquid lines of descent in basalt from the Shatsky Rise. *J Petrol* 57:309–344
- Ionov DA, Chanefo I, Bodinier J-L (2005) Origin of Fe-rich lherzolites and wehrlites from Tok, SE Siberia by reactive melt percolation in refractory mantle peridotites. *Contrib Miner Petrol* 150:335–353. <https://doi.org/10.1007/s00410-005-0026-7>
- Jarosewich E, Nelen JA, Norberg JA (1980) Reference samples for Electron Microprobe analysis. *Geostandards News* 4:43–47
- Jochum KP, Nohl U, Herwig K, Lammel E, Stoll B, Hofmann AW (2005) GeoReM: a new geochemical database for reference materials and isotopic standards. *Geostand Geoanal Res* 29:333–338. <https://doi.org/10.1111/j.1751-908X.2005.tb00904.x>
- Jousselin D, Mainprice D (1998) Melt topology and seismic anisotropy in mantle peridotites of the Oman ophiolite. *Earth Planet Sci Lett* 164:553–568
- Jousselin D, Morales LF, Nicolle G, Stephant M, A (2012) Gabbro layering induced by simple shear in the Oman ophiolite Moho Transition Zone. *Earth Planet Sci Lett* 331–332:55–66. <https://doi.org/10.1016/j.epsl.2012.02.022>
- Jousselin D, Nicolas A, Boudier F, Reisberg L, Henri M, Nicolle M (2021) Formation of the Moho transition zone in the Oman ophiolite, and comparison with sub-moho melt lenses at fast spreading ridges. *Tectonophysics* 821:229148. <https://doi.org/10.1016/j.tecto.2021.229148>
- Kelemen PB, Shimizu N, Salters VJM (1995) Extraction of mid-ocean ridge basalt from the upwelling mantle by focused flow of melt in dunite channels. *Nature* 375:747–753
- Kelemen PB, Koga K, Shimizu N (1997) Geochemistry of Gabbro sills in the crust–mantle transition zone of the Oman ophiolite: implications for the origin of the oceanic lower crust. *Earth Planet Sci Lett* 146:475–488
- Kelemen PB, Matter JM, Teagle DAH, Coggon JA, Oman Drilling Project Science Team (2020), Site CM2: Crust–mantle transition zone and into upper mantle. In P.B., Kelemen, J.M., Matter, D.A.H., Teagle, J.A., Coggon, (Eds.), *Proceedings of the Oman drilling Project: College station, TX (International Ocean Discovery Program)*, <https://doi.org/10.14379/OmanDP.proc.2020>
- Klaessens D, Reisberg L, Jousselin D, the Oman Drilling Project Science Team (2021) Highly siderophile element and os isotope results from the structurally atypical Batin Dunite in the Wadi Tayin Massif of the Oman Ophiolite. *J Geophys Res Solid Earth* 126 e2021JB021977. <https://doi.org/10.1029/2021JB021977>
- Koepke J, Feig ST, Berndt J, Neave DA, Team ODPS (2021) Wet magmatic processes during the accretion of the deep crust of the Oman Ophiolite paleoridge: phase diagrams and petrological records. *Tectonophysics* 817:229051. <https://doi.org/10.1016/j.tecto.2021.229051>
- Koga KT, Kelemen PB, Shimizu N (2001) Petrogenesis of the crust–mantle transition zone and the origin of lower crustal wehrlites in the Oman ophiolite. *Geochim Geophys Geosyst* 2. <https://doi.org/10.1029/2000GC000132>
- Korenaga J, Kelemen PB (1997) Origin of Gabbro sills in the Moho Transition Zone of the Oman ophiolite: implications for magma transport in the lower oceanic crust. *J Phys Res* 102:729–749. 0148-0227/97/97JB-02604
- Kourim F, Rospabé M, Dygert N, Chatterjee S, Takazawa E, Wang K-L, Godard M, Benoit M, Giampouras M, Ishii K, Teagle DA-H, Cooper M-J, Kelemen PB (2022) Geochemical characterization of the Oman Crust–Mantle Transition Zone, OmanDP Holes CM1A and CM2B. *J Geophys Res Solid Earth* 127 e2021JB022694. <https://doi.org/10.1029/2021JB022694>
- Le Roux V, Tommasi A, Vauchez A (2008) Feedback between melt percolation and deformation in an exhumed lithosphere–asthenosphere boundary. *Earth Planet Sci Lett* 274:401–413. <https://doi.org/10.1016/j.epsl.2008.07.053>
- Leuthold J, Lissenberg CJ, O'Driscoll B, Karakas I, Falloon T, Klimenetyeva DN, Ulmer P (2018) Partial melting of lower oceanic crust gabbro: constraints from poikilitic clinopyroxene primocrysts. *Front Earth Sci* 6:15. <https://doi.org/10.3389/feart.2018.00015>
- Lissenberg JC, Dick HJB (2008) Melt–rock reaction in the lower oceanic crust and its implications for the genesis of mid-ocean ridge basalt. *Earth Planet Sci Lett* 271:311–325. <https://doi.org/10.1016/j.epsl.2008.04.023>
- Lissenberg CJ, MacLeod CJ, Howard KA, Godard M (2013) Pervasive reactive melt migration through fast-spreading lower oceanic crust (Hess Deep, equatorial Pacific Ocean). *Earth Planet Sci Lett* 361:436–447. <https://doi.org/10.1016/j.epsl.2012.11.012>
- Lissenberg CJ, MacLeod CJ, Bennett EN (2019) Consequences of a crystal mush-dominated magma plumbing system: a mid-ocean ridge perspective. *Philosophical Trans Royal Soc A* 377:20180014. <https://doi.org/10.1098/rsta.2018.0014>
- MacLeod CJ, Lissenberg CJ, Bibby LE (2013) Moist MORB axial magmatism in the Oman ophiolite: the evidence against a mid-ocean ridge origin. *Geology* 41:459–462. <https://doi.org/10.1130/G33904.1>
- Mainprice D, Bachmann F, Hielscher R, Schaeben H (2014) Descriptive tools for the analysis of texture projects with large datasets using MTEX: strength, symmetry and components. *Geological Society of London, Special Publication* 409, <https://doi.org/10.1144/SP1409.1148>
- Miller DJ, Abratis M, Christie D, Drouin M, Godard M, Ildefonse B, Maeda J, Weinstein A, Yamasaki T, Suzuki Y, Niino A, Sato Y, Takeda F (2009) Data report: microprobe analyses of primary mineral phases from Site U1309, Atlantis Massif, IODP Expedition 304/305. In: Blackman D K Ildefonse B John B E Ohara Y Mill D J MacLeod C J Expedition 304/305 Scientists Proc IODP 304/305 Coll Stn TX (Integrated Ocean Drill Program Manage Int Inc). <https://doi.org/10.2204/iodp.proc.304305.202.2009>
- Morishita T, Ghosh B, Soda Y, Mizukami T, Tani K, Ishizuka O, Tamura A, Komaru C, Aari S, Yang H-C, Chen W-S (2018) Petrogenesis of ultramafic rocks and olivine-rich troctolites from the East Taiwan Ophiolite in the Lichi mélange. *Mineral Petrol* 112:521–534. <https://doi.org/10.1007/s00710-017-0547-6>
- Müller RD, Srolias M, Gaina C, Roest WR (2008) Age, spreading rates, and spreading asymmetry of the world's ocean crust. *Geochim Geophys Geosyst* 9. <https://doi.org/10.1029/2007GC001743>
- Müller S, Garbe-Schönberg D, Koepke J, Hoernle K (2022) A reference section through fast-spread Lower Oceanic Crust, Wadi Gideah, Samail Ophiolite (Sultanate of Oman): Trace element Systematics and REE Crystallization temperatures - implications for Hybrid Crustal Accretion. *J Geophys Res Solid Earth* 127 e2021JB022699. <https://doi.org/10.1029/2021JB022699>
- Van den Bleeken G, Müntener O, Ulmer P (2010) Reaction processes between tholeiitic melt and residual peridotite in the uppermost mantle: an experimental study at 0.8GPa. *J Petrol* 51:153–183. <https://doi.org/10.1093/petrology/egp066>

- Nicolas A, Boudier F (1995) Mapping oceanic ridge segments in Oman Ophiolite. *J Phys Res* 100:6179–6197
- Nicolas A, Boudier F, Ildefonse B, Ball E (2000) Accretion of Oman ophiolite and United Emirates ophiolite: discussion of a new structural map. *Mar Geophys Res* 21:147–179
- Nicolle M, Jousselein D, Reisberg L, Bosch D, Stephant A (2016) Major and trace element and Sr and Nd isotopic results from mantle diapirs in the Oman ophiolite: implications for off-axis magmatic processes. *Earth Planet Sci Lett* 437:138–149. <https://doi.org/10.1016/j.epsl.2015.12.005>
- Niu Y (2021) Lithosphere thickness controls the extent of mantle melting, depth of melt extraction and basalt compositions in all tectonic settings on earth—a review and new perspectives. *Earth Sci Rev* 217:103614. <https://doi.org/10.1016/j.earscirev.2021.103614>
- O'Neill HSC, Jenner FE (2016) Causes of the compositional variability among Ocean Floor Basalts. *J Petrol* 57:2163–2194. <https://doi.org/10.1093/petrology/egx001>
- Pierce JA, Alabaster T, Shelton AW, Searle MP (1981) The Oman ophiolite as a cretaceous arc-basin complex: evidence and implications. *Philosophical Trans Royal Soc Lond Ser Math Phys Sci* 300:299–317
- Rampone E, Borghini G, Godard M, Ildefonse B, Crispini L, Fumagalli P (2016) Melt/rock reaction at oceanic peridotite/gabbro transition as revealed by trace element chemistry of olivine. *Geochim Cosmochim Acta* 190:309–331. <https://doi.org/10.1016/j.gca.2016.06.029>
- Rampone E, Borghini G, Basch V (2020) Melt migration and melt-rock reaction in the Alpine-Apennine peridotites: insights on mantle dynamics in extending lithosphere. *Geosci Front* 11:151–166. <https://doi.org/10.1016/j.gsf.2018.11.001>
- Renna MR, Tribuzio R (2011) Olivine-rich troctolites from Ligurian ophiolites (Italy): evidence for impregnation of replacive mantle conduits by MORB-type melts. *J Petrol* 52:1763–1790. <https://doi.org/10.1093/petrology/egr029>
- Rioux M, Bowring S, Kelemen P, Gordon S, Dudás F, Miller R (2012) Rapid crustal accretion and magma assimilation in the Oman-U.A.E. ophiolite: high precision U–Pb zircon geochronology of the gabbroic crust. *J Phys Res* 117(B07201). <https://doi.org/10.1029/2012JB009273>
- Rioux M, Bowring S, Kelemen P, Gordon S, Miller R, Dudás F (2013) Tectonic development of the Samail ophiolite: high-precision U–Pb zircon geochronology and Sm–Nd isotopic constraints on crustal growth and emplacement. *J Geophys Res Solid Earth* 118:2085–2101. <https://doi.org/10.1002/jgrb.50139>
- Rosenberg CL, Handy MR (2005) Experimental deformation of partially melted granite revisited: implications for the continental crust. *J Metamorph Geol* 23:19–28. <https://doi.org/10.1111/j.1525-1314.2005.00555.x>
- Rospabé M, Benoit M, Ceuleneer G, Hodel F, Kaczmarek M-A (2018) Extreme geochemical variability through the dunitic transition zone of the Oman ophiolite: implications for melt/fluid-rock reactions at Moho level beneath oceanic spreading centers. *Geochim Cosmochim Acta* 234:1–23. <https://doi.org/10.1016/j.gca.2018.05.012>
- Sanfilippo A, Dick HJB, Ohara Y (2013) Melt-rock reaction in the Mantle: Mantle troctolites from the Parece Vela ancient back-arc spreading center. *J Petrol* 54:861–885. <https://doi.org/10.1093/ptrology/egs089>
- Sanfilippo A, Tribuzio R, Tiepolo M (2014) Mantle-crust interactions in the oceanic lithosphere: constraints from minor and trace elements in olivine. *Geochim Cosmochim Acta* 141:423–439. <https://doi.org/10.1016/j.gca.2014.06.012>
- Sanfilippo A, MacLeod CJ, Tribuzio R, Lissenberg CJ, Zanetti A (2020) Early-stage melt-rock reaction in a cooling crystal mush beneath a slow-spreading mid-ocean ridge (IODP Hole U1473A, Atlantis Bank, Southwest Indian Ridge). *Front Earth Sci* 8:579138. <https://doi.org/10.3389/feart.2020.579138>
- Saper L, Liang Y (2014) Formation of plagioclase-bearing peridotite and plagioclase-bearing wehrlite and gabbro suite through reactive crystallization: an experimental study. *Contrib Miner Petrol* 167:985. <https://doi.org/10.1007/s00410-014-0985-7>
- Suhr G, Hellebrand E, Johnson K, Brunelli D (2008) Stacked gabbro units and intervening mantle: a detailed look at a section of IODP Leg 305, hole U1309D. *Geochemistry. Geophys Geosyst* 9:Q10007. <https://doi.org/10.1029/2008GC002012>
- Sun SS, McDonough WF (1989) Chemical and isotopic systematics of oceanic basalts: implications for mantle composition and processes. *Geol Soc Lond Special Publications* 42:313–345. <https://doi.org/10.1144/GSL.SP.1989.042.01.19>
- Tamura Y, Rospabé M, Fujie G, Ohira A, Kaneda K, Nichols ARL, Ceuleneer G, Sato T, Kodaira S, Miura S, Takazawa E (2022) The nature of the Moho beneath fast-spreading centers: evidence from the Pacific plate and Oman Ophiolite. *Isl Arc* 31:e12460. <https://doi.org/10.1111/iar.12460>
- Tarantola A, Valette B (1982) Generalized non-linear inverse problems solved using least-squares criterion. *Rev Geophys Space Phys* 20:219–232
- Teagle DAH, Alt JC, Umino S, Miyashita S, Banerjee NR, Wilson DS and the Expedition 309/312 Scientists, 2006. *Proceedings IODP, 309/312: Washington, DC (Integrated Ocean Drilling Program Management International, Inc.)*, 1–549. <https://doi.org/10.2204/iodp.proc.309312.103.2006>
- Tommasi A, Mainprice D, Canova G, Chastel Y (2000) Viscoplastic self-consistent and equilibrium-based modeling of olivine lattice preferred orientations: implications for the upper mantle seismic anisotropy. *J Phys Res* 105:7893–7908. <https://doi.org/10.1029/1999JB900411>
- Toomey DR, Jousselein D, Dunn RA, Wilcock WSD, Detrick RS (2007) Skew of mantle upwelling beneath the East Pacific rise governs segmentation. *Nature* 446:409–414. <https://doi.org/10.1038/nature05679>
- Tursack E, Liang Y (2012) A comparative study of melt-rock reactions in the mantle: laboratory dissolution experiments and geological field observations. *Contrib Miner Petrol* 163:861–876. <https://doi.org/10.1007/s00410-011-0703-7>
- Ulmer P (1989) The dependence of Fe²⁺-Mg cation-partitioning between olivine and basaltic liquid on pressure, temperature and composition: an experimental study to 30 kbars. *Contrib Miner Petrol* 101:261–273
- Van Achteberg E, Griffin WL, Stiefenhofer J (2001) Metasomatism in mantle xenoliths from the Letlhakane kimberlites: estimation of element fluxes. *Contribution Mineralogy Petrol* 141:397–414. <https://doi.org/10.1007/s004100000236>
- VanTongeren JA, Kelemen PB, Grove TL (2022) Temperatures and timescales of crystallization in the Mush Zone beneath fast-spreading ocean ridges. *J Geophys Res Solid Earth* 127:e2022JB024812. <https://doi.org/10.1029/2022JB024812>
- Vernières J, Godard M, Bodinier JL (1997) A plate model for the simulation of trace element fractionation during partial melting and magma transport in the Earth's upper mantle. *J Geophys Res Solid Earth* 102:24771–24784
- Villiger S, Ulmer P, Muntener O (2007) Equilibrium and fractional crystallization experiments at 0.7GPa; the Effect of pressure on Phase relations and Liquid compositions of Tholeiitic Magmas. *J Petrol* 48:159–184
- Warren JM (2016) Global variations in abyssal peridotite compositions. *Lithos* 248–251:193–219. <https://doi.org/10.1016/j.lithos.2015.12.023>
- Workman RK, Hart SR (2005) Major and trace element composition of the depleted MORB mantle (DMM). *Earth Planet Sci Lett* 231:53–72. <https://doi.org/10.1016/j.epsl.2004.12.005>

- Yang AY, Wang C, Liang Y, Lissenberg CJ (2019) Reaction between mid-ocean ridge basalt and lower oceanic crust: an experimental study. *Geochem Geophys Geosyst* 20:4390–4407. <https://doi.org/10.1029/2019GC008368>
- Zhang WQ, Liu C-Z, Dick HJB (2020) Evidence for multi-stage melt transport in the lower ocean crust: Atlantis Bank gabbroic massif (IODP Hole U1473A, SW Indian Ridge). *J Petrol* 61:egaa082. <https://doi.org/10.1093/petrology/egaa082>